Thin-Walled Structures 185 (2023) 110534

Contents lists available at ScienceDirect

Thin-Walled Structures

journal homepage: www.elsevier.com/locate/tws

Full length article

Axial compressive performance of concrete-filled steel tube stub columns with high-strength spiral confined concrete core

Peng Feng [a,*], Zhiyuan Li [a], Yichong Zou [a,b], Jia-Qi Yang [c]

[a] Department of Civil Engineering, Tsinghua University, Beijing, 100084, China
[b] China Coal Technology and Engineering Group, Beijing, 100013, China
[c] School of mechanics and civil engineering, China university of mining and technology (Beijing), Beijing, 100083, China

ARTICLE INFO

Keywords:
High-strength steel spirals
Concrete filled steel tube (CFST)
3D laser scanning
Finite element analysis
Design method

ABSTRACT

Concrete-filled steel tubes (CFSTs) are widely used as hybrid columns. However, rectangular/square CFST columns are less ductile and have lower strength than circular CFST columns. To solve this problem, a novel hybrid column, namely, a high-strength steel (HSS) spiral confined CFST (HSSS-CCFST or CCFST) column, was recently proposed and investigated in this study. The spiral confinement can enhance the axial compressive performance of concrete, including load capacity, deformability and especially secondary stiffness. Monotonic axial compressive tests were conducted on 12 CCFFT columns, a steel concrete FRP concrete (SCFC) column and a CFST column. The failure modes, failure processes and mechanical behaviour of the CCFFT columns were compared with those of the SCFC and CFST columns. The relationships between the states of the columns and the materials were analysed. In addition, 3D laser scanning was performed to obtain the deformation modes. Finite element (FE) analysis of the CCFST column was conducted using commercial finite element software (Abaqus). To improve the accuracy of the simulation, the constitutive models of spirals with different strength grades were modified using the section strip method and considering the residual stress from manufacturing; the constitutive model of concrete was also improved. The results of the FE analysis agreed well with the failure modes of the components in the CCFST and the stress–strain behaviours. A parametric analysis was conducted to determine the influence of the strength and dimension parameters, and finally, the design method of the axial load capacity of the CCFST was obtained by fitting the results from the experiments and the parametric analysis.

1. Introduction

Concrete-filled steel tube (CFST) columns are hybrid columns composed of concrete and steel with the advantages of high strength, good ductility and good fire resistance [1–3]. In addition, the steel tubes can act as a permanent framework during construction, which saves time and costs. The above advantages promote the promising application of CFST columns in practical engineering. The superior performance of the CFST column comes from the combination of steel and concrete. The concrete provides internal support to the steel tube to prevent local buckling and improve the axial strength of the steel. The steel tube confines the concrete and constrains the lateral expansion and development of cracks [4].

Circular CFST column and rectangular CFST column are two common types of columns. For an axially loaded circular CFST column, the concrete is uniformly confined, and the enhancement of the strength and ductility from the confining effect is more significant than that of a rectangular CFST column [5–7]. However, the configuration of a joint connecting a circular CFST column is too complex, and it limits their application [5–7]. It is easy to connect a rectangular CFST column and other structural members, and this facilitates the division of architectural space [8]. Additionally, the flexural performance of rectangular columns is much better than that of circular columns. However, there are also some limitations for the rectangular columns. Local buckling tends to appear earlier on the side plates of the tubes, especially away from the corners [9]. In addition, the concrete in the rectangular cross-section is under nonuniform confinement, which is inefficient [10]. Some researchers also focused on the octagonal CFST column, which has the advantage of higher confinement and ease of connection [11,12]. In conclusion, the balance between the confining effect and connection is the essential issue for CFST columns.

To enhance the performance of rectangular CFST columns, extra strengthening components are added to the columns, for example, binding bars [13], ribs [14,15], longitudinal reinforcements and circumferential reinforcements. Utilizing circumferential reinforcements

* Corresponding author.
E-mail address: fengpeng@tsinghua.edu.cn (P. Feng).

https://doi.org/10.1016/j.tws.2023.110534
Received 9 September 2022; Received in revised form 30 November 2022; Accepted 5 January 2023
Available online 21 January 2023
0263-8231/

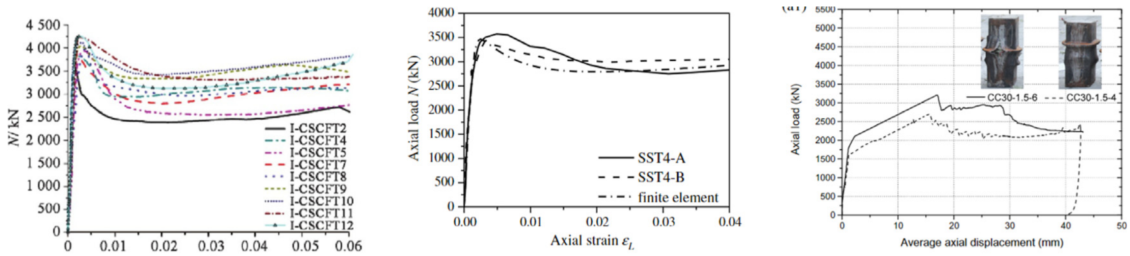

(a) CFST column with circular steel tube (Qian and Zhang et al., 2011)

(b) CFST column with normal strength spirals (Ding and Fang et al., 2014)

(c) CFST column with circular FRP tube (Feng and Cheng et al., 2015)

Fig. 1. Load–strain/displacement curves for CFST columns with different internal confinement.

in the steel tube is one of the most attractive approaches with a simple configuration. The circumferential reinforcements can provide sufficient and almost uniform confinement to internal concrete, enhancing the strength and ductility of the whole column. Based on the above mechanism, many kinds of novel hybrid columns have been proposed in recent years. Qian et al. proposed rectangular CFST columns with circular steel tubes and investigated their axial compressive (as shown in Fig. 1(a)) and seismic performance [16,17]. The columns proposed by Qian et al. showed good deformability and residual strength. Their failure was characterized by local buckling and rupture of the corners of the external rectangular tube, local buckling of the internal circular tube and crushed concrete between the tubes. Ding et al. presented a comparative study of the axial compressive performance of CFST columns with internal loops or spiral stirrups and inner stiffeners and found that CFST columns with spirals were superior to others with the same steel consumption (as shown in Fig. 1(b)) [18–20]. Feng et al. proposed a novel concept for an FRP-confined concrete core (FCCC) and utilized it in a CFST column, namely, a steel concrete FRP concrete (SCFC) column [21–23]. The FRP tube provided sufficient and constant confinement, and thus, the SCFC column showed significant bilinear behaviour, i.e., post-yield hardening (PYH) behaviour (shown in Fig. 1(c)). PYH behaviour is common in axial compression tests of FRP-confined concrete and flexural tests of FRP-strengthened beams, and members with such behaviour are superior to those with elastic-brittle or elastic–plastic behaviours. Feng et al. suggested a design philosophy for members with PYH behaviours, which will be more widely applied in the future [24]. SCFC columns show PYH behaviour because the FRP tube has almost linear-elastic behaviour with a large rupture strain and can provide a continuously increasing confining stress. While, for the CFST columns with extra steel circumferential reinforcements, the confining stress is constant after the circular steel tubes or the normal strength spirals yield.

Teng et al. recently proposed a rectangular CFST column with high-strength steel (HSS) spirals, i.e., an HSS spiral-confined concrete-filled steel tube (HSSS-CCFST or CCFST) [25,26]. High-strength spirals yielded at a higher strength than normal-strength spirals and provided sufficient confinement. Compared with FRP tubes, the high-strength spirals have financial advantages, a larger fracture strain, and might be more attractive for practical applications. To investigate the comprehensive performance of CCFST columns, a joint research programme was undertaken by the Hong Kong Polytechnic University and Tsinghua University. An experiment including CCFST columns, CFST columns, high-strength steel spiral-confined columns and hollow steel tubes was reported by Teng et al. The test results showed that the CCFST specimens were much more ductile than the other specimens. Finally, a design method based on the superposition method was proposed, which could provide a conservative prediction.

To reveal the mechanism of the CCFST columns more clearly, monotonic axial compressive tests were conducted on 12 CCFFT columns, 1 SCFC column and 1 CFST column in this study. The experimental parameters included the strength and spacing of the spirals and the use of longitudinal reinforcement. The failure modes, failure process and mechanical behaviour of the CCFFT columns were obtained and compared with those of the SCFC and CFST columns. The relationships between the states of the columns (yield point, peak and residual branch) and the materials (lateral dilation of concrete, local buckling of steel tubes, yield and fracture of spirals) were analysed. In addition, 3D laser scanning was performed on the columns to obtain the deformation modes and processes. Based on the 3D laser scanning results, the effect of the extra confinement (spiral or FRP tube) on CFST columns was analysed graphically. A finite element (FE) analysis of the CCFST column was conducted using commercial finite element software (Abaqus). To improve the accuracy of the simulations, the constitutive models of spirals with different strength grades were modified based on the section strip method and considering the residual stress from manufacturing, which was generally neglected in existing literature for spiral-confined concrete; the constitutive model of concrete was also improved. The FE results agreed well with the failure modes of the components in the CCFST and the stress–strain behaviours. A parametric analysis was conducted to obtain the influence of the strength and the dimension parameters, and finally, a design method of the axial load capacity of the CCFST was obtained by fitting the experimental results and the results from the parametric analysis.

2. Experimental preparation

2.1. Test specimens

The test specimens included 14 square columns composed of 12 CCFFT columns, 1 SCFC column and 1 CFST column. The dimensions of all the specimens were 500 mm (height) and 170 mm (side length). The cross-sections of the three types of specimens are shown in Fig. 2. The SCFC column and CFST column were set as the reference specimens for the type of confinement. For the CCFST columns, the experimental parameters involved the spacing of the spirals (20 and 40 mm), the strength of the spirals (HPB300, CRB600 and CRB800) and the use of the longitudinal reinforcement (with or without).

The list of specimens is shown in Table 1. For the CCFST, the format of the specimen ID is [Type]-[Spacing]-[Spiral strength]. The specimen ID starts with the letter "CC" to represent a CCFST column, followed by a hyphen and a two-digit number to represent the spacing of the spirals and then another hyphen and a one-digit number to represent the strength of the spirals; some of them end with the letter "L" to represent the use of longitudinal reinforcement. The numbers "1", "2", and "3" indicate that the grades of the spirals were HPB300, CRB600 and CRB800, respectively. The names of the SCFC column and CFST column were given by two characters: "SC" and "CF". In addition, there was a repeated specimen for specimen CC-20-3, and the repeated specimen was named "CC-20-3*".

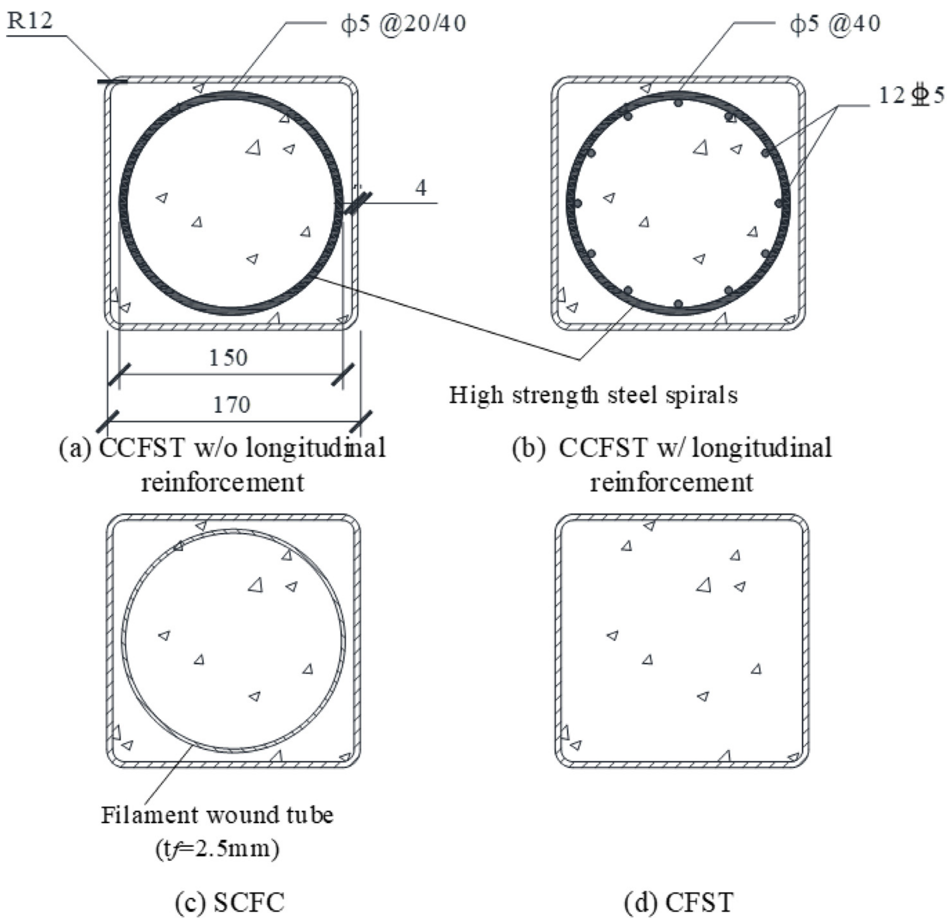

Fig. 2. Sections of the specimens for axial compression tests.

Table 1
Test matrix.

Specimens	Total volumetric reinforcement ratio	Longitudinal reinforcement	Spacing of spirals	Grade of spirals
CC-20-1	1.76%	/	20 mm	HPB300
CC-20-2	1.76%	/	20 mm	CRB600
CC-20-3	1.76%	/	20 mm	CRB800
CC-20-3*	1.76%	/	20 mm	CRB800
CC-40-1	0.88%	/	40 mm	HPB300
CC-40-2	0.88%	/	40 mm	CRB600
CC-40-3	0.88%	/	40 mm	CRB800
CC-40-1L	1.76%	12Φ5	40 mm	HPB300
CC-40-2L	1.76%	12Φ5	40 mm	CRB600
CC-40-3L	1.76%	12Φ5	40 mm	CRB800
CC-15-2	2.35%	/	15 mm	CRB600
CC-15-3	2.35%	/	15 mm	CRB800
SC	Filament wound tube (t_f = 2.5 mm)			
CF	/	/	/	/

2.2. Material properties

All the tubes were groove welded by two cold-formed “C” section steel plates with a thickness of 4 mm and grade of Q235. All the steel plates were delivered in one batch. Dog-bone shaped coupons were cut from steel plates from the same batch and tested under uniaxial tensile loading according to *Metallic materials — Tensile testing -Part 1: Method of test at room temperature* [27]. The results from the material property test are listed in Table 2.

All the specimens were cast using one batch of commercial precast concrete with a target strength of 40 MPa. Six cubes with a side length of 150 mm were cast and tested under compressive loading according to the *Standard for Evaluation of Concrete Compressive Strength* [28]. After curing for 28 days, the cube strength was 47.6 MPa, and the cylinder strength was 38.9 MPa according to Cheng and Feng et al. [23]

The spirals in the CCFST specimens with a diameter of 5 mm were prepared by winding rebars on circular steel tubes. This ensured that the external diameter of the helix (after the springback process) was 150 mm. The spacings of the spirals were 15, 20, and 40 mm in this study. In addition, for the spirals with a spacing of 40 mm for each strength grade, two spirals were manufactured, and one was welded on the longitudinal reinforcements with the same grade and quality as the corresponding spirals. The volume percentages of the spirals and the longitudinal reinforcements were both 0.88%. Five specimens were cut from rebars for each strength grade and tested under uniaxial tensile loading according to *Metallic materials — Tensile testing -Part 1: Method of test at room temperature* [27]. The results from the material property tests are listed in Table 2, and the stress-strain curves are shown in Fig. 3.

The GFRP tube in the SCFC specimen was made by a filament winding process; it had a diameter of 150 mm, a thickness of 2.5 mm and a winding angle of 85°. The GFRP tube was composed of E51 epoxy resin and 2400Tex glass fibre. The hoop tensile modulus, ultimate strength and ultimate strain were 45.2 GPa, 907.3 MPa and 2.04%, respectively; they were obtained from the hoop tensile test according to the *Standard Test Method for Apparent Hoop Tensile Strength of Plastic or Reinforced Plastic Pipe* [29].

2.3. Test setup and instrumentation

The axial compression tests were conducted using a hydraulic compression testing machine with a loading capacity of 5000 kN; the test

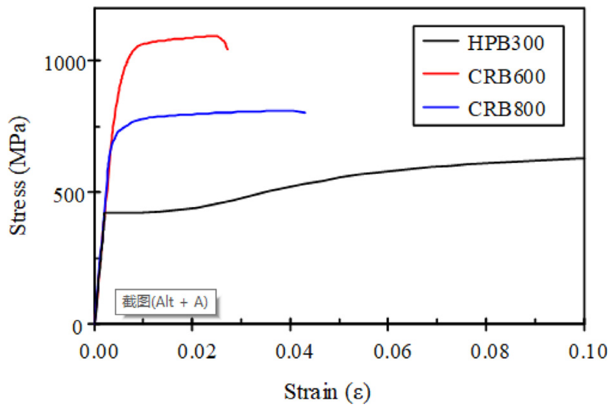

Fig. 3. Stress–strain curves of the rebars/spirals under uniaxial tensile loading.

Table 2
Test results from the material property tests.

Material	Yield stress (MPa)	0.2% proof stress (MPa)	Tensile strength (MPa)	Percentage elongation at fracture (%)
Q235B	270.0	/	412.3	32.0%
HPB300	422.6	/	484.8	24.1%
CRB600	/	747.3	807.9	4.0%
CRB800	/	1028.4	1078.1	2.5%

setup is shown in Fig. 4(a). The two ends of each specimen were plastered with mortar before the test, and then the specimen was installed in the testing machine. The central axis of the specimen coincided with the loading axis of the testing machine according to laser calibration. To avoid local failure at the ends, two steel fixtures were arranged at the top and bottom of each specimen.

Linear differential displacement transducers (LVDTs), strain gauges and 3D laser scanning were adopted to monitor the deformation of the specimens. Four vertical LVDTs were installed between the loading surfaces of the testing machine to measure the axial displacement, as shown in Fig. 4(b). Six strain rosettes were mounted at the outer surface of steel tubes to measure the local deformation, and eight strain gauges were mounted at the spirals for the CCFST specimens. The strain rosettes and the strain gauges were all in the mid-height section of the columns. All data were collected synchronously with the force transducer on the testing machine at a frequency of 1 Hz.

During the test, a load-controlled loading scheme was applied first to all the specimens with a loading rate of 50 kN/min, and then the loading scheme was changed to displacement control with a loading rate of 1 mm/min when the specimens approached their yield points.

3. Experimental results

3.1. General behaviour and failure modes

During the tests, the specimens with various configurations showed different behaviours. The loading stages and corresponding behaviours of different specimens are described below:

CFST column. The experimental process for the CFST column was divided into four stages: (1) In the elastic stage, there was no obvious behaviour. (2) In the post-yield hardening stage, local buckling of the steel tube was observed, and bulging was observed near the mid-height of the column. (3) In the descending stage, the applied load decreased after the peak until reaching the residual load. Two wave crests formed gradually on each side of the steel tubes, and shear deformation patterns were observed in the specimen. (4) In the residual stage, the applied load remained stable, and the load increased slightly with increasing deformation. When the axial deformation reached approximately 40 mm (the axial strain was 8%), a vertical crack caused by lateral tensile stress appeared at the corner of the steel tube. Then, the load decreased instantly, and the test was terminated. The failure modes were characterized by local buckling of the steel tube and shear deformation patterns, and the behaviour was classified as a ductile failure.

SCFC column. The experimental process for the SCFC column was divided into four stages: (1) In the elastic stage, there was no obvious behaviour. (2) In the 1st post-yield hardening stage, local buckling of the steel tube, was observed, and bulging gradually developed into two wave crests on each side as the test progressed. (3) In the 2nd post-yield hardening stage, the load continued to increase with a more gradual slope, and some cracking sounds were heard. This was because with the continuous confinement from the FRP tube, the internal concrete bore the load drop caused by the local buckling of the steel tube, and the load kept increasing. (4) In the descending stage, a loud sound was heard at an axial deformation of 10 mm, and the load dropped instantly, indicating hoop rupture of the FRP tube. In addition, owing to the presence of the FRP tube, shear deformation patterns did not appear in the SCFC column. (5) In the residual stage, the applied load maintained the residual load, which was higher than that of the CFST column. Similarly, the load increased slightly with increasing deformation. When the axial deformation reached approximately 30 mm (the axial strain was 6%), a vertical crack was observed at the corner, and the load decreased instantly at the same time. Through the cracking, the concrete between the steel tube and the FRP tube was crushed to powder. The failure modes were characterized by hoop rupture of the FRP tube and crushed concrete.

CCFST columns without longitudinal reinforcements The experimental process of the CCFST column without longitudinal reinforcements was divided into five stages (shown in Fig. 5): (1) In the elastic stage, there was no obvious behaviour. (2) In the post-yield hardening stage, similar to the SCFC column, local buckling of the steel tube was observed, and bulging developed in two wave crests on each side. (3) In the platform stage, the load continued to increase with a much more gradual slope. This stage was different from that of the SCFC column, which was related to the yield of the spirals and thus, the time when this stage appeared was related to the spacing and the strength of the spirals. (4) In the descending stage, several sounds were heard as the load dropped step by step for the specimens with CRB600 or CRB800, which indicated a fracture of the spirals. (5) In the residual stage, the applied loads maintained residual loads, which were different for various specimens, and all values were greater than that of the CFST column. In addition, shear deformation patterns were found in the CCFST columns without longitudinal reinforcements. At the end of testing, most specimens had a vertical crack at the corner that developed when the axial deformation reached approximately 30 mm (the axial strain was 6%). However, specimen CC-20-2 had a vertical crack at the welding line at axial deformation of 20 mm. The failure modes were characterized by fracture (with CRB600 or CRB800) or yield (with HPB300) of the steel tubes. Shear deformation patterns were not included in the failure modes, which appeared in the residual stage instead of the descending stage.

CCFST columns with longitudinal reinforcements: The experimental process of the CCFST column with longitudinal reinforcements was divided into four stages because there was no platform stage. The behaviours in the elastic stage and the post-yield hardening stage of the CCFST columns with longitudinal reinforcements were similar to those of the CCFST columns without the reinforcements. However, the buckling of the longitudinal reinforcements promoted shear slip deformation patterns and influenced the contribution to the axial load from the utilization of the spirals; thus, there was no platform stage. The failure modes were characterized by the buckling of the longitudinal reinforcements and the shear deformation patterns.

To observe the failure modes of the internal concrete, the steel tubes were removed, as shown in Fig. 6. For all the columns, the concrete

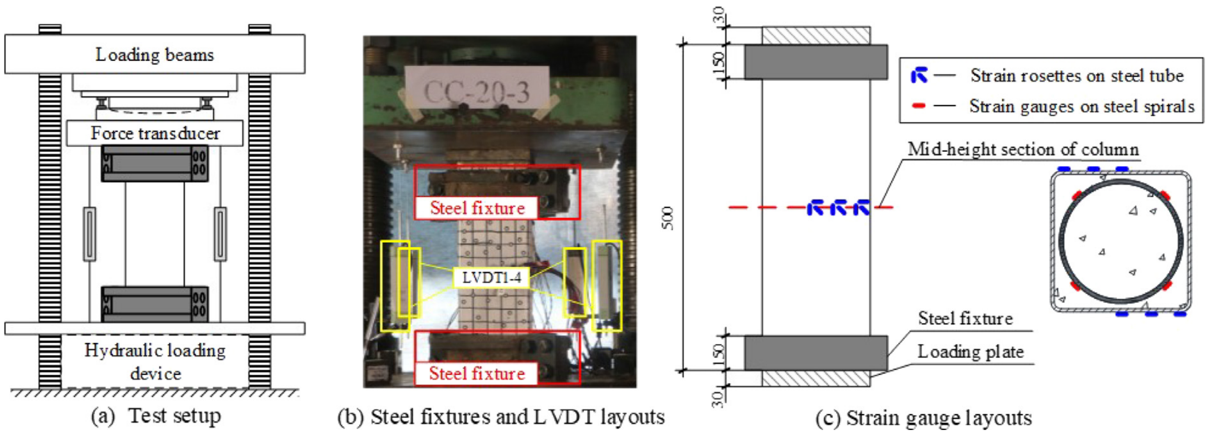

Fig. 4. Test setup and instrumentation: (a) test setup, (b) steel fixtures and LVDT layout and (c) strain gauge layout.

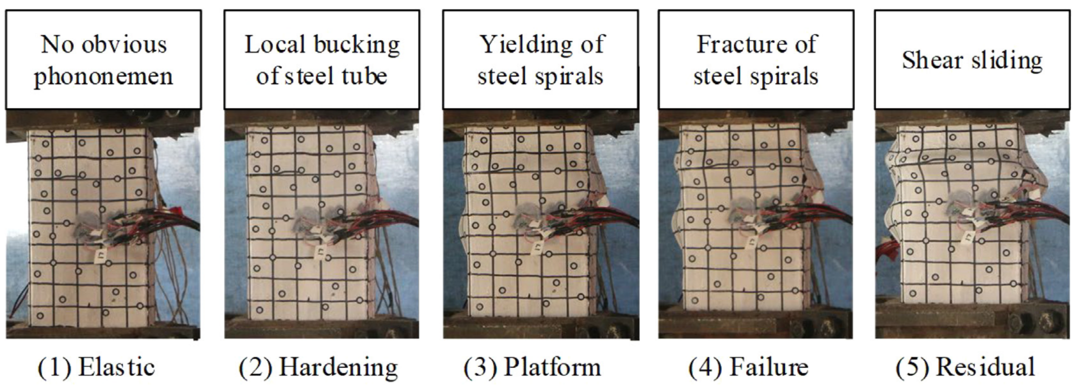

Fig. 5. Failure process of a typical CCFST specimen.

near the wave crests was crushed into grains, which indicated that the local buckling of the steel tubes influenced the confining effect. Furthermore, the sandwich concrete was also removed to find the deformation patterns of the internal confining materials and concrete. For the SCFC column, the FRP tubes ruptured, and a zigzag crack was observed, as shown in Fig. 6(b). For the CCFST columns without longitudinal reinforcements, there were several fractures on the spirals, but the internal concrete remained intact, as shown in Fig. 6(c). For the CCFST columns with longitudinal reinforcements, the longitudinal reinforcements buckled under the compressive load, as shown in Fig. 6(d). For some of the CCFST columns, the shear slip deformation was so distinct that the connected shear cracks formed a shear-slip surface, as shown in Fig. 6(e). The formation of the shear-slip surface was related to the distribution of the fractures on the spirals. In the case that the distribution of the fracture was along a diagonal line, the shear cracks could connect. In the case of the distribution of the fracture in a vertical line, the shear cracks were restrained by the spirals, and the shear slip surface did not form.

3.2. Load–strain behaviours

The load-average strain curves of all the specimens are plotted in Fig. 7. The strains were the averages of the readings of 4 LVDTs, and the values in the elastic stage were modified according to the readings of 6 strain rosettes. The curves were sorted into four groups according to the configurations: (a) the specimens with only spirals with a spacing of 20 mm; (b) the specimens with only spirals with a spacing of 40 mm and the SCFC specimen; (c) the specimens with spirals with a spacing of 40 mm and longitudinal reinforcements; and (d) the specimens with only spirals with a spacing of 15 mm. The curve of the CFST column was plotted in all four figures for ease of comparison.

The yield points of all the curves corresponded to the local buckling of the steel tubes, and after that, the curves for different groups showed various behaviours. (1) Group a: the hardening stage was not obvious, and the influence of the strength of the spirals on the curves was not distinct. The spacing of the spirals was too large to provide enough confinement and limit the propagation of cracks, which provided very little strength enhancement. As the test processed, the CRB600 and CRB800 spirals fractured, which was accompanied by small load drops. The HPB300 spirals did not fracture, and the load decreased slowly. Finally, the curves entered the residual stage, and the residual loads for the specimens in Group a were similar. (2) Groups b and d: owing to smaller spacing and resulting higher confining stiffness, the load–strain curves showed significant post-yield hardening behaviour. With the increase in the yield strength of the spirals, the secondary hardening branch was more obvious. Then, the spirals yielded and provided continuous confining pressure with the internal concrete, and thus, the curves entered the platform stage. They remained in the platform stage until the first fracture of the spiral occurred. The load dropped step by step, corresponding to the fracture of the spirals one by one. Finally, the curves entered the residual stage, and the load tended to increase, which was not considered due to the low slope and large deformation in this stage. (3) Group c: the stress–strain curves also showed post-yield hardening, but the secondary stiffness decreased more obviously than in the other cases. Most importantly, there was only a sharply descending stage after the peak instead of a platform stage because the longitudinal reinforcements buckled, which influenced the confining effect of the spirals. Although the peak load of Group c was similar to that of Group d, Group c was less ductile. Adding more materials did not result in better performance. After the load decreased by different degrees, the step-by-step load drop corresponding to one-by-one fractures was observed, and the curves ended in the residual stage.

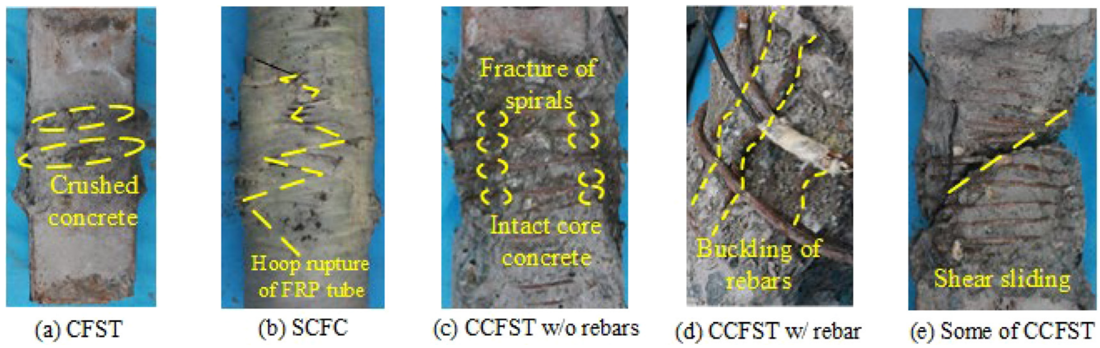

Fig. 6. Internal failure modes of specimens.

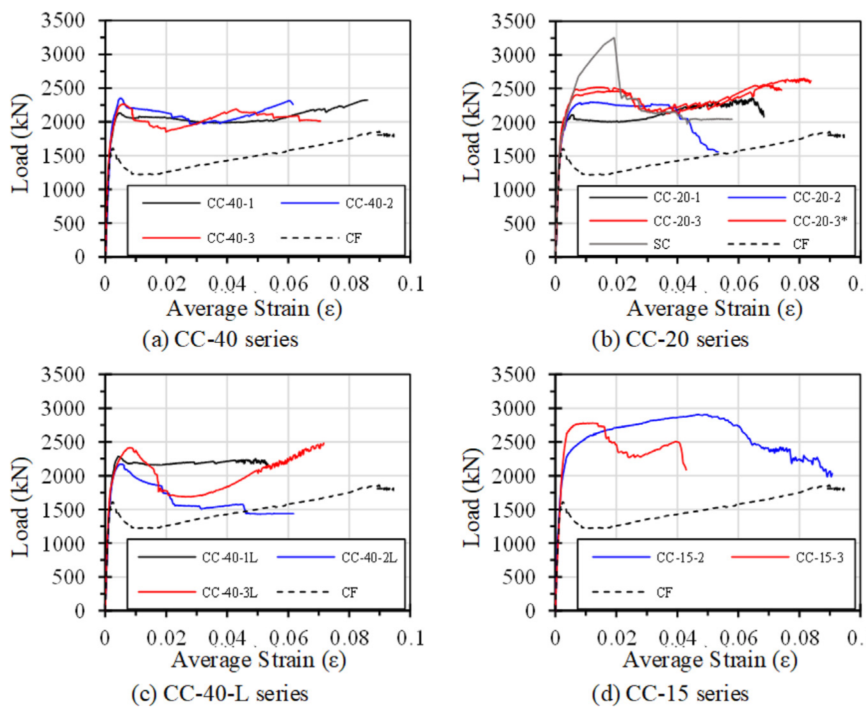

Fig. 7. Load-average strain curves of the specimens under axial compression.

Compared with the CFST specimens, the CCFST specimens had better mechanical performance, which indicated that the introduction of the spirals contributed to improving the weak confinement of the CFST specimen. Compared with the SCFC specimens, the CCFST specimens had similar secondary stiffness but lower peak strength and a stable platform stage. This was related to the different mechanical behaviours of the steel spirals and the FRP tube. The FRP tube showed linear elastic behaviour in the hoop direction and provided a confining pressure that increased continuously. The spirals had almost ideal elastoplastic behaviour and provided constant confining pressure. The curves in the descending stage were also different. When the FRP tube almost ruptured, the load of the SCFC specimen reached the peak and then decreased sharply. However, the spirals fractured one by one, and thus, the load of the CCFST specimens dropped step by step.

Table 3
Key results of the axial compressive tests.

Specimen	P_y (kN)	ε_y (με)	P_p (kN)	ε_p (με)	P_r (kN)
CC-20-1	1790	1860	2111	5420	2006
CC-20-2	1810	2570	2301	11 410	1561
CC-20-3	1887	3570	2465	18 670	2145
CC-20-3*	1853	3360	2522	13 830	2123
CC-40-1	1550	1570	2133	4710	1986
CC-40-2	1780	1820	2352	5050	1970
CC-40-3	1583	1410	2266	5550	1853
CC-40-1L	1761	1780	2287	4300	2152
CC-40-2L	1767	1880	2172	4910	1432
CC-40-3L	1777	1880	2416	8180	1687
CC-15-2	2289	4280	2911	46 820	1986
CC-15-3	2463	3140	2782	17 920	2088
SC	1745	3280	3256	18 990	1976
CF	1356	1120	1610	2310	1217

3.3. Quantitative results

Quantitative results were extracted from the load–strain curves to compare the key parameters of the different specimens, as listed in Table 3. The key parameters included the yield point, peak and residual point. The yield point was determined by the Farthest Point Method suggested by Feng et al. [30]. The peak point corresponded to the maximum load. The residual point was the lowest point in the residual stage.

Graphical comparisons of the key states are given in Fig. 8. The yield strengths of most CCFST and SCFC specimens were approximately 400 kN larger than that of CFST specimens. When the spacing decreased

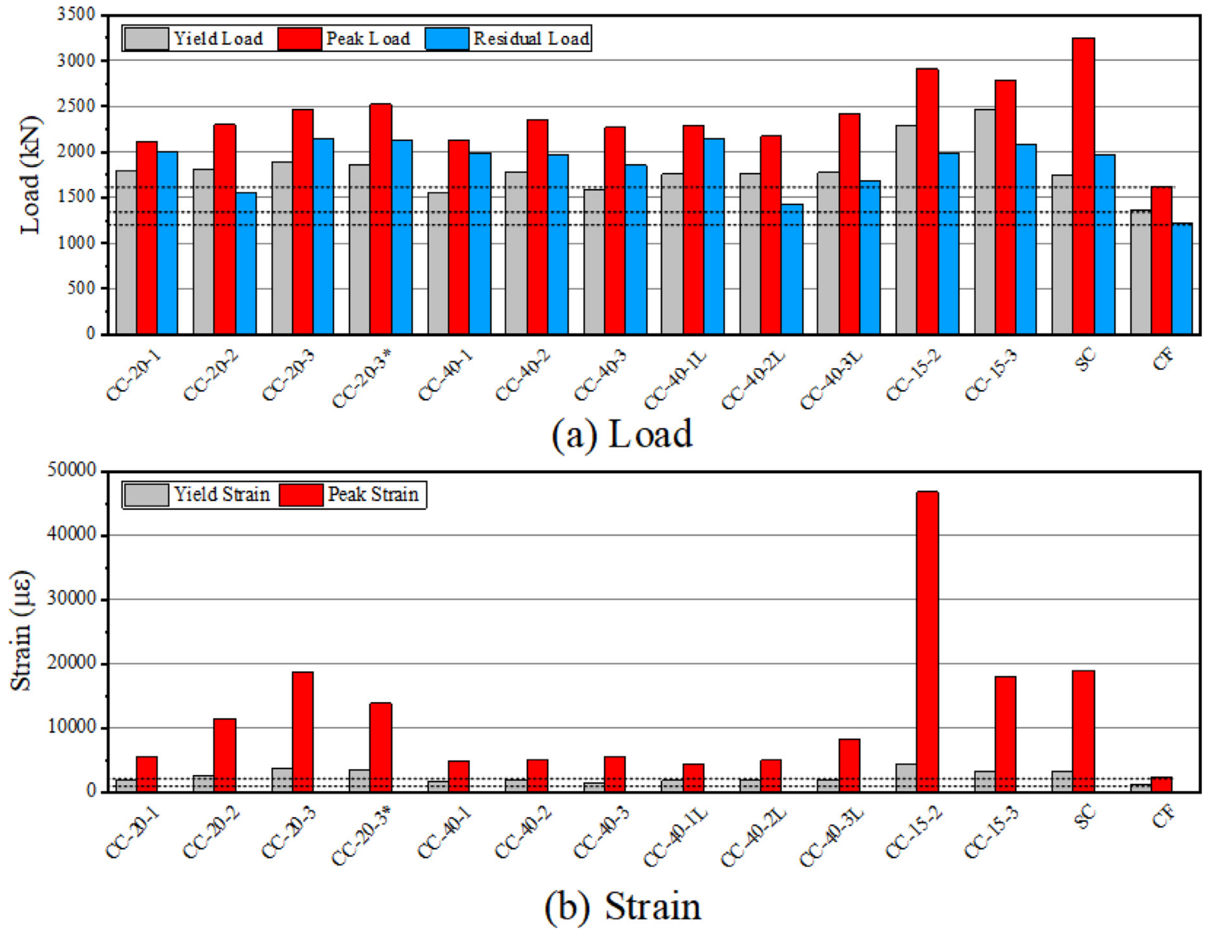

Fig. 8. Comparison of the key results for the specimens.

to 15 mm, the yield strengths were 1000 kN larger. The introduction of the spirals and the FRP tubes enhanced the peak strength more distinctly, and the enhancement ranged from 31.1% to 80.8%. The residual strengths for the CCFST and SCFC specimens were also much larger, but the enhancement was not as distinct as that of the peak strengths. Notably, the introduction of longitudinal reinforcements increased the residual strength. The average residual load for Group a was 1967 kN, while that for Group c was 1757 kN.

The yield strains of all specimens were close to 5000 με, indicating that the extra confining materials made relatively small contributions to the yield point. The strain enhancement for the CCFST specimens ranged from 86% to 708%, and the specimens were divided into two types. For the CC-20-1, CC-40-1, CC-40-2, CC-40-3, CC-40-1L and CC-40-2L specimens, the peak strains were less than 10 000 με. This was related to weak confinement of the internal concrete; the post-yield hardening behaviour was not distinct. For the CC-20-2, CC-20-3, CC-20-3*, CC-40-3L, CC-15-2 and CC-15-3 specimens, the spirals with greater strength and higher volumetric ratios, i.e., more confinement, were utilized, and the peak strains were larger than 10 000 με. Among them, the peak for the CC-15-2 specimen appeared in the middle of the platform stage, and the strain reached 46 820 με.

3.4. Behaviour of steel spirals

The measured strains of steel spirals for two typical specimens (CC-40-3 and CC-20-3) are presented in Figs. 9 and 10, respectively.

Fig. 9 shows the load–strain relationships during the whole test. In Fig. 9, the curves are plotted in two forms; the full and the dashed lines represent the strains before and after the first fracture, respectively. In addition, two straight lines are plotted for comparison; they represent the yield of the column (blue dashed line) and that of the spirals (red dashed line). As shown in the figures, the behaviour of the spirals shared a similar tendency as follows: (1) in the elastic stage, the strain was at a low level, which indicated that the microcracks in the concrete did not develop much, and lateral expansion was not obvious. (2) As the test processed, the columns yielded, and the concrete expanded laterally considerably, which led to a distinct increase in the spirals. Because the spirals were still in unyielded conditions, the lateral confining stress and the load continued to increase. (3) When the spirals yielded, the lateral confining stress became constant, and the load increased more slowly until the peak load. The strains of the spirals increased rapidly due to plastic development, and they exceeded the measuring range in some cases. (4) In the descending stage, the first fracture occurred, and the load decreased considerably. For the strain gauges near the fracture, the strains/stress were unloaded. For the strain gauges away from the fracture, the strain continued to increase due to the expansion of the concrete and friction between the concrete and spirals. The confining stress remained in some areas of the columns, which explained why the residual loads of the CCFST specimens were greater than that of the CFST specimen.

Fig. 10 shows the strain distributions in the key states. Four measured strains were similar in different states, indicating that the internal concrete was under a uniform confined condition. Uniform confinement could ensure full use of the confining materials and enhance the performance of confined concrete.

3.5. Influence of steel spirals

The concrete confined by steel spirals shared the same mechanism as the FRP confined concrete. To analyse the influence of steel spirals,

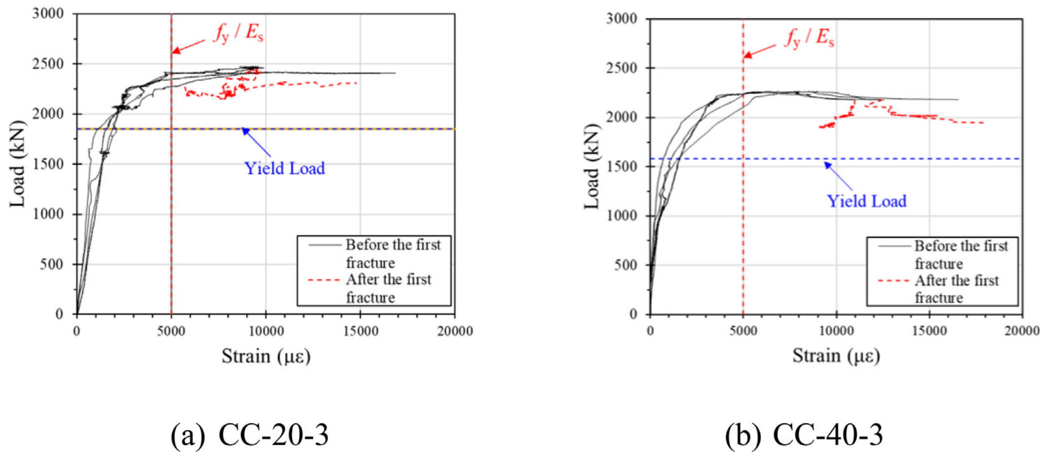

Fig. 9. Load–strain relationships of spirals. (For interpretation of the references to colour in this figure legend, the reader is referred to the web version of this article.)

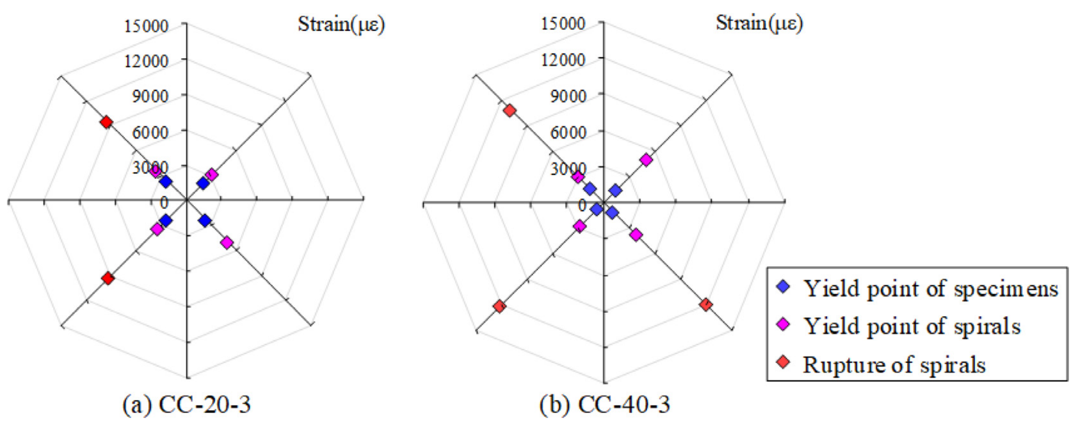

Fig. 10. Strain distributions of spirals.

the concept of the strength confinement ratio was introduced. This ratio was proposed by Teng et al. to analyse the influence of FRP composites based on the principle of force balance [30]. The yield strength confinement ratio was calculated by a similar method, as shown in Fig. 11. Notably, the spirals were helixes, and there were angles between the axis of the spirals and the hoop direction. Hence, the lateral confining stress was equal to the projection of the tensile force in the cross section of the columns. The yield strength confinement ratio is given as follows:

$$\zeta = \frac{f_{l,y}}{f_{co}} = \frac{2f_{yh}A_{sp}cos\theta}{Ds} * \frac{1}{f_{co}} = \frac{2f_{yh}A_{sp}}{f_{co}Ds}\frac{\pi D}{\sqrt{(\pi D)^2 + s^2}} = \frac{2f_{yh}A_{sp}}{f_{co}s\sqrt{D^2 + \left(\frac{s}{\pi}\right)^2}} \tag{1}$$

where f_{yh} is the yield strength of the spirals, A_{sp} is the area of the spiral, D is the external diameter of the helix and f_{co} is the strength of the concrete. To exclude the influence of longitudinal reinforcement, only the results for the CCFST specimens without longitudinal reinforcement were calculated and are listed in Table 4. The concrete in the CCFST columns was not only under confinement by the spirals but also under hybrid confinement by the spirals and tubes. The variable ΔN was calculated to analyse the enhancement by the spirals. To exclude the enhancement by the tubes, the load at the peak strain of the CCFST specimen in the load–strain curve of the CFST specimen was extracted. ΔN was equal to the peak load of the CCFST specimen minus the extracted load. The relationship between ΔN and the yield strength confinement ratio is plotted in Fig. 12. There was a significant positive correlation between them, which indicated that the contribution to the peak load increased linearly with the increase in the yield strength confinement ratio.

Table 4
Yield confinement ratio.

Specimen	D (mm)	s (mm)	A_{sp} (mm^2)	f_{yh} (MPa)	ζ	ΔN (kN)
CC-20-1	150	20	19.635	484.75	0.162	753
CC-20-2	150	20	19.635	807.9	0.271	1068
CC-20-3	150	20	19.635	1038.1	0.349	1242
CC-20-3*	150	20	19.635	1038.1	0.349	1301
CC-40-1	150	40	19.635	484.75	0.081	716
CC-40-2	150	40	19.635	807.9	0.135	959
CC-40-3	150	40	19.635	1038.1	0.174	916
CC-15-2	150	15	19.635	807.9	0.362	1456
CC-15-3	150	15	19.635	1038.1	0.465	1551

3.6. 3D laser scanning

3D laser scanning is an innovative noncontact measuring method that uses laser transmitters to accurately record the shape of a static object and a dual charge-coupled device (CCD) to save the data in the form of a point cloud [31]. In this study, 3D laser scanning was conducted to measure the shapes of the specimens in key states. When the applied load reached a certain value, the loading machine was controlled to stay at constant displacement. The specimens, with markers that had been applied before the tests, were scanned by a handheld device. After the scanning process, the loading machine continued to increase the load. The scanning process influenced the load-strain curve. While the specimens were in the plastic stage, the load tended to

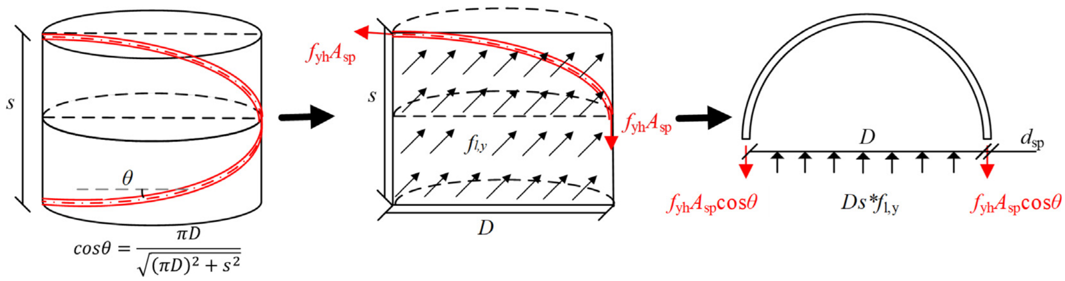

Fig. 11. Diagrams for the calculation of the yield confinement ratio of spirals.

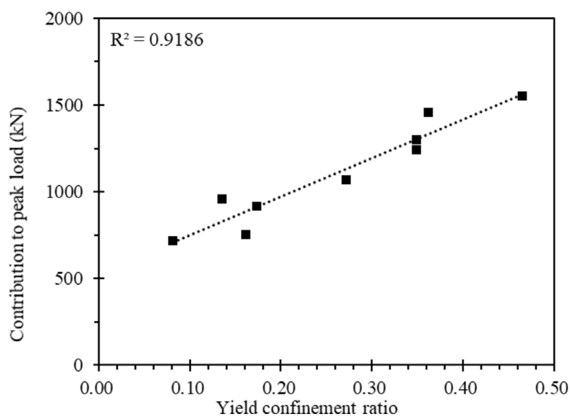

Fig. 12. Correlations between the peak load and the yield confinement ratio.

decrease when the specimen was maintained at constant displacement, as shown by the decreases in the red circles in Fig. 13(a). The scanning process was brief; it was completed within 3 min, and it did not influence the curves.

The point cloud that represented the external surface of each specimen from the 3D laser scanning was recorded by sets of 3D coordinates. The measured data were processed further by commercial software or programs developed in this laboratory. In this study, noise reduction and triangulation were conducted on the point cloud by commercial software, Geomagic Studio 2014. The full process of the deformation of a typical CCFST column is presented graphically in Fig. 13(b), which was rendered by commercial software, Rhinoceros.

To present the deformation patterns more clearly and directly, the 2D outlines of important sections in key states were extracted from the 3D models. The rules for determining the important sections are presented in Fig. 14. The cross sections were the sections where the wave crest was located, and the vertical sections were the sections where the lateral deformation (mainly shear sliding) was located. The outlines of the important sections of the typical CCFST, SCFC and CFST specimens are shown in Fig. 15. Some essential conclusions can be summarized by comparing the outlines: (1) In the elastic stage, the three specimens did not undergo deformation. (2) During the post-yield hardening stage, bulges appeared in the vertical sections, and the outlines of the cross sections expanded slightly, indicating the onset of the local buckling of the steel tubes. Notably, the deformation patterns were nonsymmetric; two wave crests were present at different heights. (3) In the platform stage/2nd hardening stage and subsequent failure stage, the local buckling developed further, and the bulges were more obvious. In addition, the rectangular corners tended to open and become round, which was also reported by Cheng et al. in the experimental investigation of SCFC columns.

(4) In the residual stage, the steel spirals or the FRP tubes fractured, and the deformation patterns varied. For the CCFST specimens, the fractured spirals could not prevent shear deformation on the diagonal section, and the specimens showed shear sliding patterns. The central axis deviated greatly from the original position. A similar phenomenon was observed on the CFST specimen, and it appeared earlier. For the SCFC specimens, the ruptured FRP tubes were intact in most areas, which limited the development of shear deformation. Only slight flexural and shear deformations were observed on the central axis. The failure of the internal confining materials led to an increase in concrete expansion, and the external steel tubes bore more lateral stress. More wave crests developed in the steel tubes under the combination of axial and lateral deformations. The new crests were more obvious for the CCFST specimens and CFST specimen, which was related to the shear sliding deformation patterns.

As shown in Fig. 7, for most specimens, the residual stage was followed by a stress recovery stage. This is related to the changes of the cross-sections during the loading process. As shown in Fig. 15, the corners of the rectangular columns were open and the cross-sections were more like circles. The confinement from the external tube became higher, resulting in the stress recovery stage. The axial strains of the stress recovery stage generally exceed 5%, which is much higher than possible strain in practical engineering. Therefore, this stage will not be discussed further in this paper.

In conclusion, local buckling occurred in all types of columns; it first appeared in the post-yield hardening stage and then developed continuously. The extra confining materials (spirals and FRP tubes) effectively limited the development of microcracks. Thus, the deformation patterns were mainly axial compression, and shear sliding was postponed. The prevention of shear sliding ended after the fracture of the spirals for CCFST specimens and lasted longer for the SCFC specimen.

4. Finite element analysis

4.1. Constitutive model

4.1.1. Steel spiral

The steel spirals used in this study were manufactured by a cold forming process. First, the end of the original material was welded on a steel tube with a specific size, which was fixed on a lathe. The other end of the material was set on a traction device that maintained a certain tensile stress. Then, the steel tube (internal mould) was rotated by the lathe, and the material was wound on the steel tube. The strain and stress distributions after the winding process are shown in Fig. 16(a). The steel in the edge region of the section entered the plastic stage. When the steel had been wound for enough cycles, it was cut off, and springback occurred. The strain and stress distributions after springback are shown in Fig. 16(b). In this process, the moment of the section was unloaded to 0. The strain and stress decreased in proportion to the distance from the central axis. However, due to plasticity, the stress distribution after the winding process was not linear with the distance from the central axis, and thus, the stress distribution had a more complicated pattern. Finally, the spacing of the spirals was adjusted, and they were fixed by welding with #4 steel wire (diameter 5.893 mm) in the longitudinal direction.

The yield strengths differed for the spirals of various grades, which led to different behaviours in the winding and springback processes.

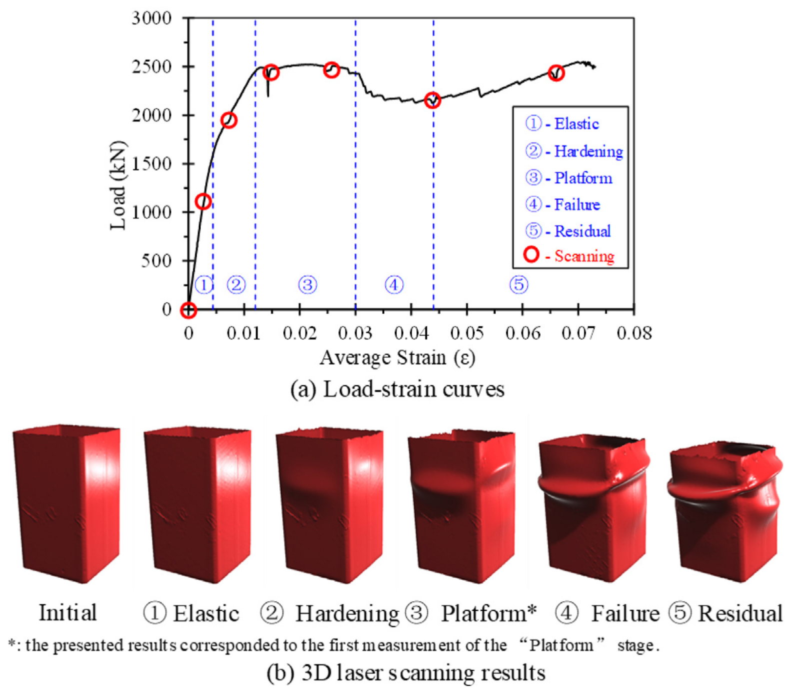

Fig. 13. Stages examined by 3D laser scanning and corresponding results.

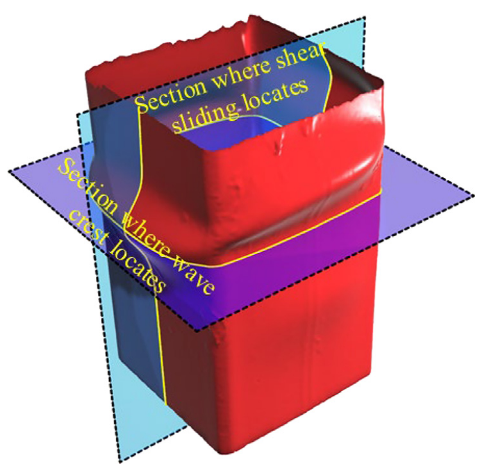

Fig. 14. Diagrams of the extracted sections.

The springback was more severe for the high-strength spirals because their elastic limit was higher, and more steel in the section was in the elastic stage. To make spirals with higher grade have the same outer diameter of the helix, an internal mould with a smaller diameter was adopted, which meant the moment/curvature in the winding process was higher and more plasticity developed. The residual stress caused by plasticity was more distinct. To simulate the winding and springback processes and quantitatively analyse the plastic development, residual stress and their influence on the hoop tensile behaviour, a section strip method was conducted. By this method, the diameters of the mould were predicted, and the hoop tensile behaviours of the spirals were modified.

(1) Section strip division: The section strip division is shown in Fig. 17(a). The neutral axis was taken as the X-axis, and the axis perpendicular to the neutral axis was taken as the Y-axis. The section was divided by several straight lines parallel to the Y-axis. The width (b_i) of the ith strip was calculated from the height (yi):

$$b_i = \sqrt{d_{sp}^2 - 4y_i^2} \tag{2}$$

Table 5
Simulated results of the manufacturing process.

Grade of rebars	Diameter of rebar d_{sp} (mm)	Diameter of helix D (mm)	Simulated diameter of mould $D_m - d_{sp}$ (mm)	Experimental diameter of mould $D_m - d_{sp}$ (mm)
HPB300	5	147.5	119	130
CRB600	5	147.5	108	120
CRB800	5	147.5	95	110

(2) Constitutive model: The loading envelope was determined on the tested results of the origin materials under uniaxial tension. The unloading and reloading curves were consistent with the model proposed by Légeron et al. [32], as shown in Fig. 17(b).

(3) Loading regime: The loading regime included four states and three loading stages, as shown in Fig. 17(c). At the first state, the strain and curvature were zero. Then, the moment (M_m) was applied on the section in the winding stage, and the curvature changed to ϕ_m (the second state). After that, the moment was unloaded in the springback stage, and the curvature changed to ϕ_k (the third state). ϕ_k corresponded to the expected diameter of the helix (D). Finally, hoop tensile load was applied to simulate the hoop tensile load from the expansion of concrete in CCFST columns. The average stress–strain relationship in the loading stages was simply the modified hoop tensile behaviour of the spirals.

The section strip method was used to predict the diameters of the mould, and they are listed in Table 5. There were differences between the simulated and experimental values. This was related to the model of Légeron et al. in which Bauschinger's effect was assumed to occur, which led to the overestimation of the deformation in the springback stage. In addition, the axial strain in the neutral axis in the winding stage was assumed to be zero, and there was only a moment and no tensile load in the section. However, in fact, the traction device applied a tensile load on the spirals, which led to errors in simulating the development of plasticity.

The modified hoop tensile behaviours for the spirals with different grades were compared with the tensile behaviours of the original materials, as shown in Fig. 18. For the high-strength spirals, the softening

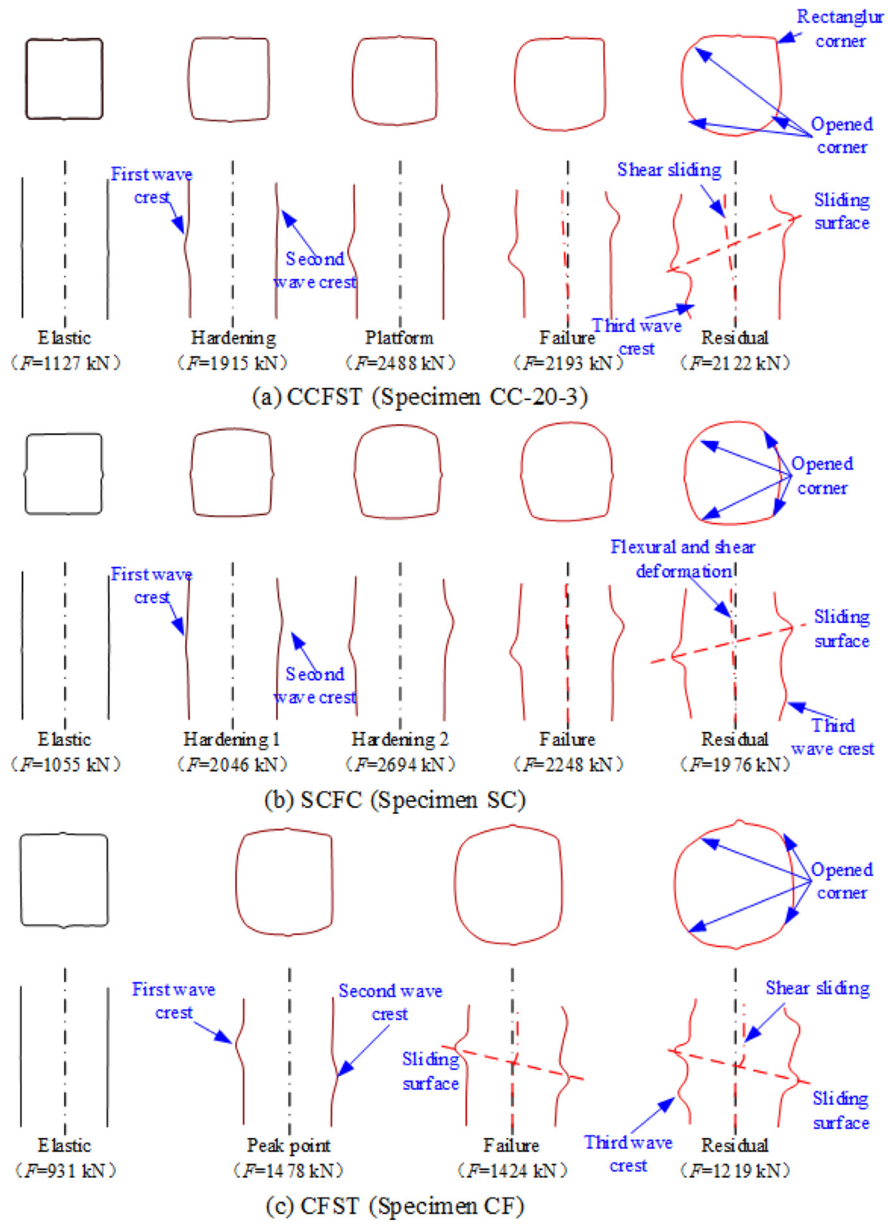

Fig. 15. Comparison of the results of the CCFST, SCFC and CFST specimens.

behaviour in the modified tensile stage appeared earlier than in the uniaxial tensile behaviour. However, similar behaviour did not occur for the HPB300 spirals, and the modified tensile behaviour was the same as the uniaxial tensile behaviour.

Based on the modified hoop tensile behaviours, the axial stress–plastic strain relationships for the spirals were calculated and input into the FE software. A sharply descending branch was added to the stress–strain relationship to simulate the fracture of the spirals.

4.1.2. Concrete

To simulate the concrete confined by spirals, a modified plastic-damage model within the framework of the concrete damage plastic model (CDPM) was adopted in the FE models. The modified plastic-damage model was proposed by Yu et al. and used to simulate the behaviour of actively confined concrete, uniformly passively confined and nonuniformly confined concrete [33,34]. The modifications of the CDPM included a damage parameter, a strain-hardening/softening rule and a flow rule, which were realized by the user-defined subroutine in the user-defined field (USDFLD). Solution-dependent field variables were defined to simulate the changes in the material properties depending on the confining pressure and the rate of the confining pressure increment. The detailed methods of the modified CDPM in Abaqus can be found in Yu et al. [34]. The values of the damage variables in Yu et al.'s study were calculated from the stress–strain according to the model of Teng et al. [35]. Subsequently, Jiang and Teng proposed another theoretical model based on more experimental data, which was proven to be superior to the model of Teng et al. [36]. Hence, the values of the damage variable were also calculated from the stress–strain relationship in the model of Jiang and Teng in a subsequent study by Wang [37]. Wang found that it was necessary to improve the model of Jiang and Teng at higher confining stiffness [37]. The improvement was achieved by modifying the model of the lateral expansion of confined concrete. Therefore, the authors followed Wang's method and modified Jiang and Teng's model by proposing a novel axial strain–lateral strain relationship and calculated the damage variable to carry out the FE analysis. Yang and Feng's study gave a 3D interpretation of the theoretical model and proposed the classification for the confined concrete according to its confining stiffness, which contributed to the modification in this paper [38–40].

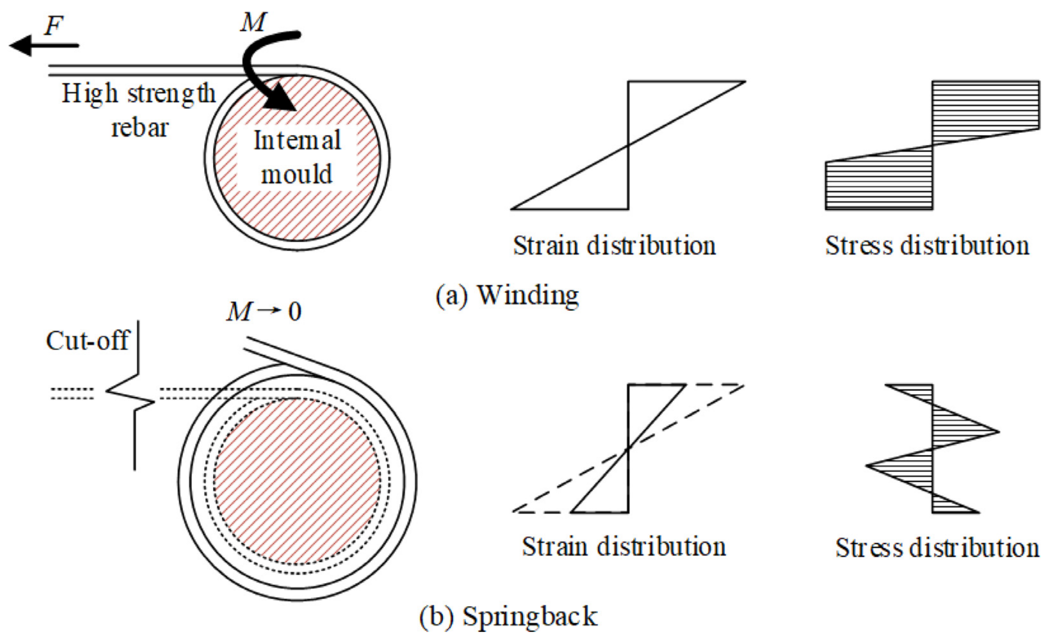

Fig. 16. Manufacturing process and corresponding stress/strain distribution.

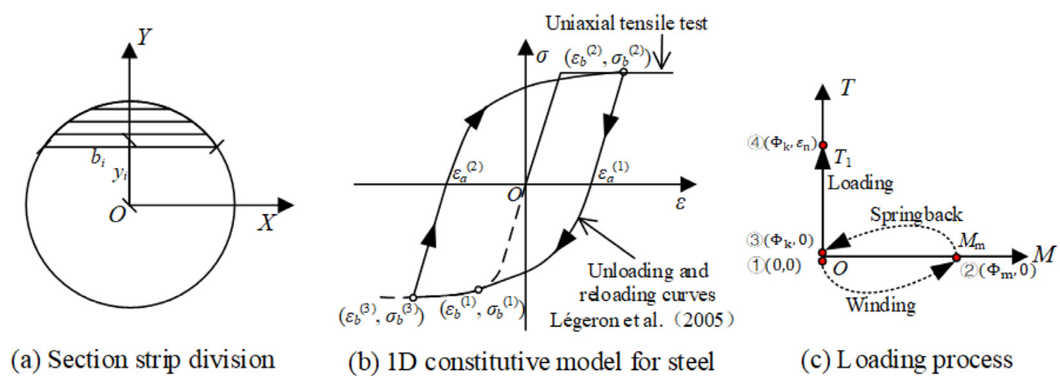

Fig. 17. Section strip model for steel spirals.

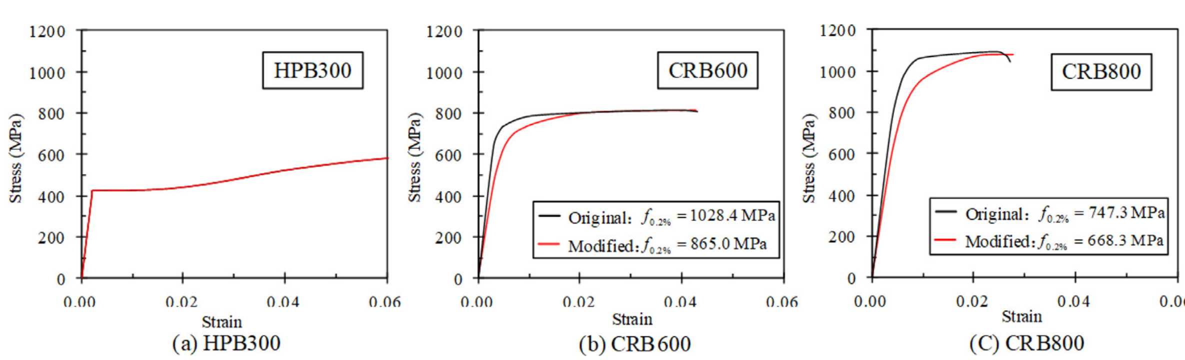

Fig. 18. Modified stress–strain relationships of spirals.

The spirals used in the CCFST columns provided lateral confining stress with a maximum of 30 MPa, and thus, the CCFST columns were classified as concrete under extremely high lateral confining stress. Therefore, it was necessary to modify the axial strain–lateral strain relationship to obtain a better simulation. Based on the fact that the initial Poisson's ratio was constant, a novel axial strain–lateral strain relationship was proposed in this paper, as shown below:

$$\varepsilon_l = \begin{cases} -\mu\varepsilon_c & 0 \le \varepsilon_c < \varepsilon_{dlt} \\ -\mu\varepsilon_c - \dfrac{A\left(\frac{\varepsilon_c}{\varepsilon_{dlt}}-1\right)^{2c}}{B+\left(\frac{\varepsilon_c}{\varepsilon_{dlt}}-1\right)^{c}} & \varepsilon_c \ge \varepsilon_{dlt} \end{cases} \tag{3a}$$

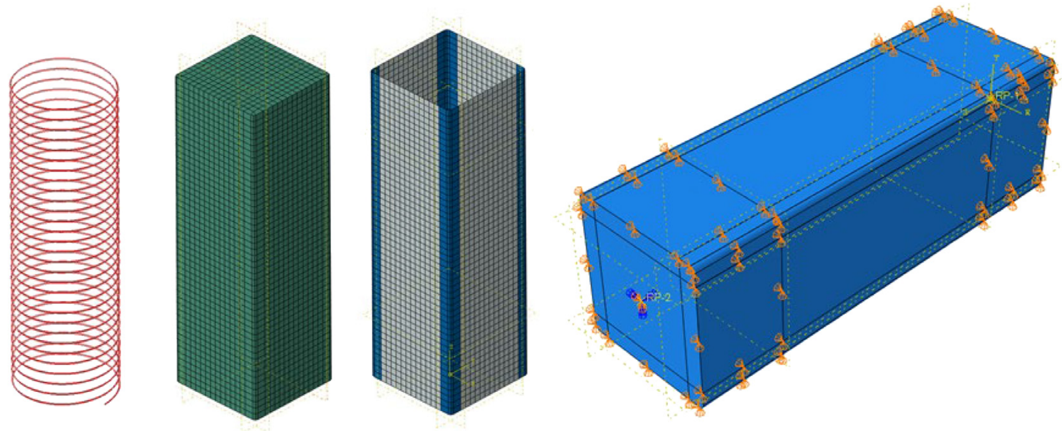

(a) Parts and corresponding mesh (b) Boundary conditions

Fig. 19. FE model.

$$\varepsilon_{dlt} = (0.6 + 3.4\frac{\sigma_l}{f'_{co}})\varepsilon_{co} \tag{3b}$$

where ε_{dlt} is the critical axial strain corresponding to the limit of lateral dilation. When the axial strain exceeded the limit, the concrete began to expand laterally and nonlinearly. Parameters A and B controlled the curvature near the critical point, and parameter C controlled the nonlinearity of the dilation. The recommended values for parameters A, B and C were 1.3, 2.0 and 1.2, respectively. The axial stress–axial strain relationships for confined concrete with different confining stiffnesses were obtained by combining the proposed axial strain–lateral strain relationship and the axial stress–axial strain relationship for confined concrete with a constant confining stress proposed by Teng et al. [35]. The modification to the model had been verified by the experimental data in existing literatures [41], which is not introduced in this paper for brevity. The modified model predicts essentially the same results as Jiang and Teng's model in the case with low confining stiffness. While, in the case with high confining stiffness, the modified model's prediction for the concrete's lateral dilation is more accurate. In conclusion, the modified model has better applicability for the cases with different confining stress.

Based on the proposed model and the method proposed by Yu et al., the parameter list to modify the CDM was obtained. To verify the modified CDM, a single-element model with the element of C3D8R was established in Abaqus and used to simulate actively confined and passively confined concrete. The single-element test is given below: (1) establishing a single-element model; (2) adopting the modified CDP model with the damage variables from the theoretical model as the constitutive model; (3) setting boundary conditions (for actively-confined concrete, a given stress is applied; for passively-confined concrete, supports with a given stiffness are applied); (4) output the axial-stress–strain curve and compare it with the origin theoretical model. The results from the FE analysis agreed well with the results from the numerical simulation, which indicated that the behaviour of the concrete was the same in the FE model and the proposed model.

4.2. FE modelling

Considering the dimensions and the stress state of the components, three kinds of elements in Abaqus were adopted to simulate the behaviour of the spirals, tubes with rectangular cross section and concrete. The diameters of the spirals were very small compared with their lengths, and the spirals mainly bore tensile loads during the tests; thus, a two-node beam element (B31) was adopted for the spirals. The thickness of the rectangular tube was very small compared with their side length and height, and thus, a four-node shell element with reduced integration (S4R) was adopted for efficiency. An incompatible mode eight-node brick element with three degrees of freedom (C3D8I) was used to simulate the concrete. The meshed parts are shown in Fig. 9. Notably, the cross sections of the tubes were rounded rectangles, and there were two lines of elements near each rounded corner.

A surface-to-surface contact with the normal behaviour of the "hard contact" relationship and the tangent behaviour of "penalty" stiffness were used to simulate the interface between the concrete and the tube. The "hard contact" relationship allowed interfacial separation, which contributed to simulating the local buckling of the tube. The "penalty" simulated friction between the concrete and the tube, and the friction coefficient was 0.5. The spirals were set to be "embedded" in concrete, meaning there was no slippage between the concrete and the spirals. The constraint was acceptable for this study because there was no slippage before the fracture of the spiral, and this constraint provided good calculation efficiency.

The boundary conditions in this model included the loading boundaries and the constrained boundaries, as shown in Fig. 19(b). "Partitions" were processed near the ends of the columns, and the partitioned area corresponded to the area constrained by the steel fixtures. The lateral displacement was constrained for the side surfaces of this area. The top and bottom surfaces were set to be "coupling" to reference points, and the axial load was applied by setting the axial displacement of the reference points.

A stress perturbation and bucking mode calculation were conducted on the model. The first three buckling modes were assigned to the model as initial imperfections, and the amplitude was 1/100 of the thickness of the tube (0.04 mm).

4.3. Model verification

The "static, general" procedure considering geometric nonlinearity in Abaqus/Standard was conducted on the model. The load–strain relationships and the failure modes of the parts were extracted from the model. The load–axial strain relationships from the FE analysis are shown in Fig. 20 and compared with those from the experiments. The experimental relationship for the CCFST column with high-strength spirals showed the post-yield hardening, platform and descending stage, which corresponded to the local buckling of the tubes, the yield of the spirals and the fracture of the spirals, respectively. Similar load–strain behaviour and phenomena were also observed in the FE model. The load–hoop strain of the HSS spiral relationships from the FE analysis are shown in Fig. 21 and compared with those from the experiments. It could be found that the spirals in FE analysis worked earlier than those in experiments, which is related to the overestimation of lateral expansion of concrete. Generally, the yield of spirals corresponds to the

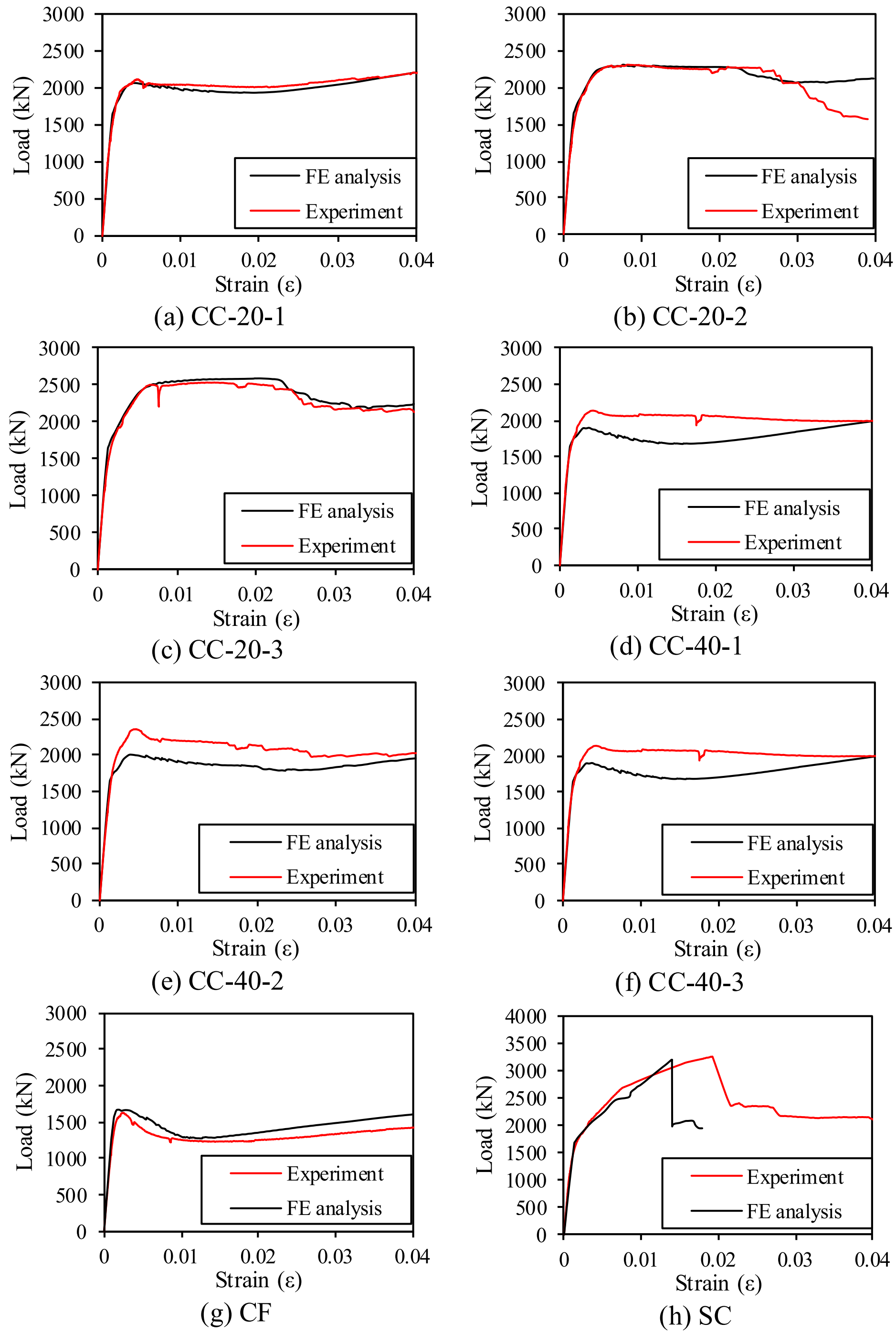

Fig. 20. Comparison of the load–axial strain curves from experiment and FE analysis.

peak load, which proved the contribution from the spirals to the axial behaviour of the CCFST columns.

The failure modes of the parts in the model are shown in Fig. 22. Hoop fracture occurred in some areas of the spirals, as shown in Fig. 22(a). The deformation patterns of the tubes were symmetric, and bulges were located near the steel fixtures, as shown in Fig. 22(b), which was different from the nonsymmetric deformation patterns observed in the experiments. The shear slipping patterns did not disappear in the FE model. This was related to the insufficient randomness introduced into the model, including the randomness of the materials and the randomness of geometry. However, the model was capable of simulating the behaviour of the concrete under hybrid confinement. The internal concrete confined by the spirals and the tubes expanded less than the concrete between the tubes, as shown in Fig. 22(c).

In conclusion, the FE models established in this section provided relatively accurate predictions of the load–strain behaviour of confined concrete, and they provided a basis for further study.

4.4. Parametric analysis

Based on the model verified in the previous section, a parameter analysis was conducted to investigate the influence of the parameters that were not involved in the experiment. The investigated parameters included the thickness of the tubes (2, 4, 6 and 8 mm), the strength of the tubes (300, 400, 500 and 600 MPa) and the external diameter of

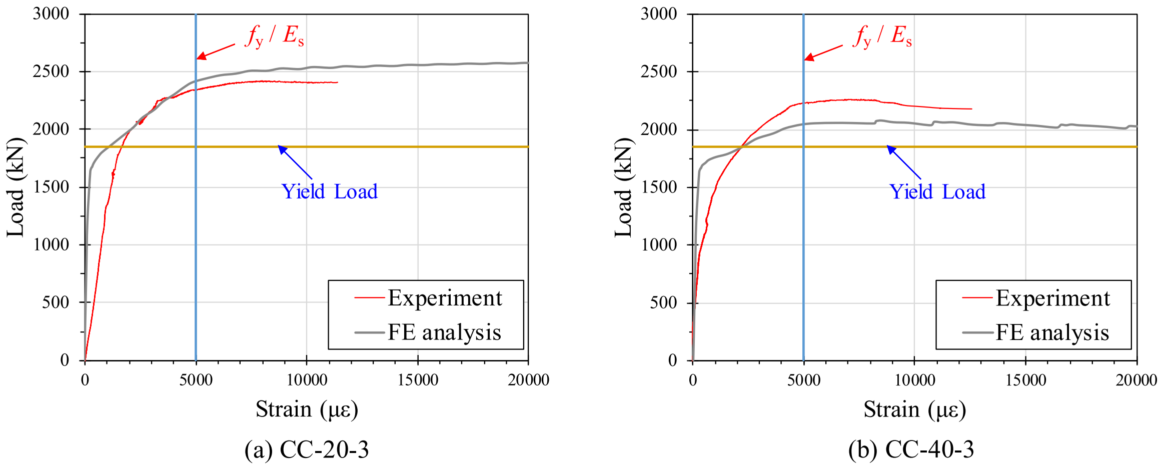

Fig. 21. Comparison of the load–hoop strain curves from experiment and FE analysis.

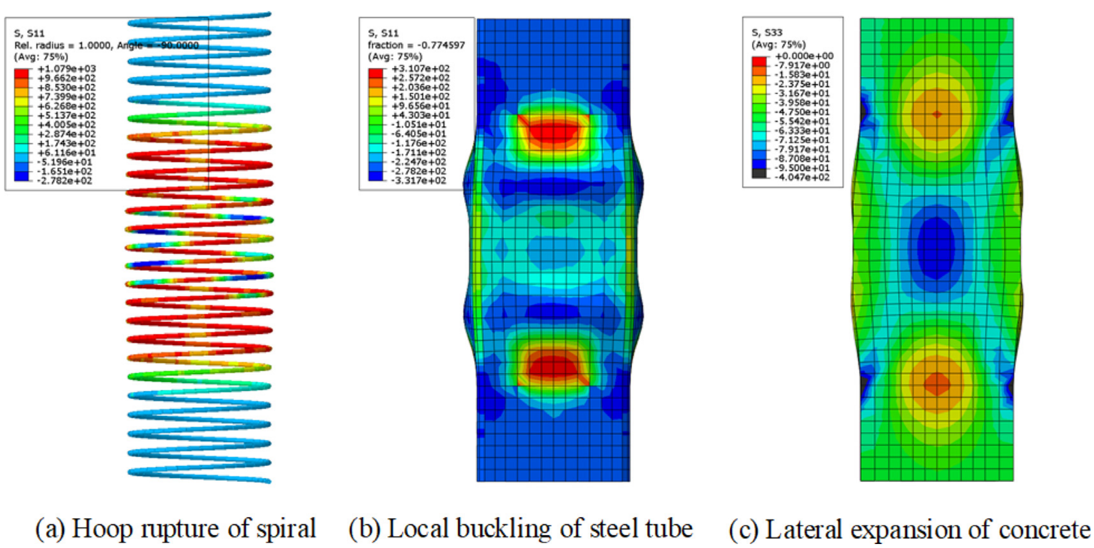

Fig. 22. Failure modes of parts in the FE model.

the helix (90, 120 and 150 mm). The other design parameters of the model in this section adopted the parameters of the CC-20-3 specimen.

Fig. 23(a) shows the load–strain relationships for the CCFST columns with different tube thicknesses. With increasing thickness, the initial stiffness, yield load, peak load and residual load increased continuously. The increase was related to not only the increase in the cross-sectional area but also the postponed local buckling.

Fig. 23(b) illustrates the influence of the strength of the tubes on the load–strain relationships. With increasing strength, the yield load, peak load and residual load all increased. However, the post-yield hardening stage was less obvious because the decrease in the steel strength caused by local buckling was greater for high-strength steel, and the steel strength was not used more fully.

Fig. 23(c) shows the load–strain relations for the CCFST columns with helixes with different diameters. The initial stiffness and the yield load were almost unchanged. However, the secondary stiffness and the peak load distinctly decreased. This parameter changed the confining stiffness ratio and the area of the internal confined concrete. To ensure significant post-yield hardening behaviour, the area of the internal confined concrete should be sufficient, and the diameter of the helix should be large enough.

4.5. Design method

A design equation for the axial load capacity of the CCFST columns was proposed in this paper. Notably, the axial load capacity in the design method was the peak load of the columns corresponding to the yield of the spirals.

The design equation included the dimensional parameters (side length (B) and thickness (t) of the tubes, diameter of the spirals (d_{sp}), spacing (s) and diameter (D) of the helix) and the material parameters (yield strength of the tubes (f_y), yield strength of the spirals (f_{yh}) and strength of the concrete (f_{co})). The equivalent width to thickness ratio ($\sqrt{\alpha_s}$), which was used to evaluate the confinement of the steel tubes and proposed by Sakino et al. and the yield strength confinement ratio (ζ), which was used to evaluate the confinement of the spirals, were applied to reduce the complexity of the equation. The yield strength confinement ratio was given by Eq. (1), and the equivalent width to thickness ratio was calculated from the following equation:

$$\sqrt{\alpha_s} = \frac{B}{t}\sqrt{\frac{f_y}{E_s}} \tag{4}$$

Hence, the design equation is given as follows:

$$N = \left(a_1 - a_2\sqrt{\alpha_s}\right) f_y A_s + a_3 f_{co} A_{sc} + (1 + a_4\zeta) f_{co} A_{cc} \tag{5}$$

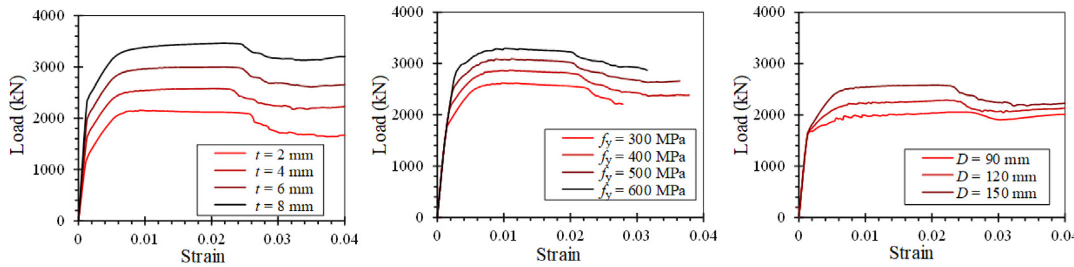

(a) Effect of the thickness of steel tube (b) Effect of the strength of steel tube (c) Effect of the diameter of helix

Fig. 23. Load–strain curves.

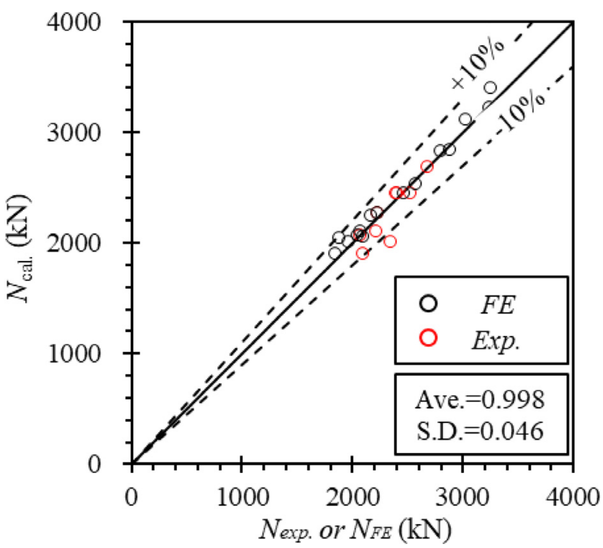

Fig. 24. Comparison of the experimental, FE and calculated results.

where A_s is the area of the steel tube, A_{sc} is the area of the sandwich concrete and A_{cc} is the area of the internal confined concrete. $a_1 \sim a_4$ are dimensionless coefficients and determined by data fitting: $a_1 = 1.287$, $a_2 = 0.1199$, $a_3 = 0.7279$, and $a_4 = 2.817$. The experimental and FE results and those calculated by the design method are compared in Fig. 24 and listed in Appendix A. The errors did not exceed 10%, except for the CC-40-2 specimen, which indicated that the design method was capable of providing accurate predictions.

4.6. Comparisons with current design methods

Current codes provided design methods for the axial compressive strength of rectangular CFST members. Comparisons with design methods suggest in ANSI/AISC 360-16 [42] and GB 50936-2014 [43], which are introduced below, were shown in this paper.

(1) ANSI/AISC 360-16

A series of design equations are provided in ANSI/AISC 360-16 to estimate the cross-sectional strength of CFST columns (N_{AISC}). The CFST columns could be classified into three groups, i.e. Compact, Noncompact and Slender, depending on the width–thickness-ratio (b/t) of the steel tube.

First, N_{p} and N_{y} should be calculated, as shown below:

$$N_p = f_y A_S + 0.85 f'_c (A_c + A_{sr}\frac{E_S}{E_c}) \tag{6a}$$

$$N_y = f_y A_S + 0.7 f'_c (A_c + A_{sr}\frac{E_S}{E_c}) \tag{6b}$$

(1a) For compact sections

$$N_{AISC} = N_p \tag{6c}$$

(1b) For noncompact sections

$$N_{AISC} = N_p - \frac{N_p - N_y}{(\lambda_r - \lambda_p)^2}(\lambda - \lambda_p)^2 \tag{6d}$$

(1c) For slender sections

$$N_{AISC} = f_{cr} A_S + 0.7 f'_c (A_c + A_{sr}\frac{E_S}{E_c}) \tag{6e}$$

$$f_{cr} = \frac{9E_S}{(b/t)^2} \tag{6f}$$

where, A_{sr} is the area of the steel rebar. ($\lambda_p = 2.26\sqrt{\frac{E_S}{f_y}}$) is the critical value between Compact and Noncompact. ($\lambda_r = 3.00\sqrt{\frac{E_S}{f_y}}$) is the critical value between Noncompact and Slender.

(2) GB 50936-2014

The axial compressive strength can be calculated according to the equations below:

$$N_{GB} = A_{sc} f_{sc} \tag{7a}$$

$$f_{sc} = (1.212 + B\theta + C\theta^2) f_c \tag{7b}$$

$$\theta = \frac{A_s}{A_c} * \frac{f_y}{f_c} \tag{7c}$$

$$B = \frac{0.131 f_y}{213} + 0.723 \tag{7d}$$

$$C = -\frac{0.070 f_y}{213} + 0.026 \tag{7e}$$

The compared results are listed in Appendix B. It could be seen that the averages of ($N_{\mathrm{exp.}}/N_{\mathrm{AISC}}$ or $N_{\mathrm{FE}}/N_{\mathrm{AISC}}$) and ($N_{\mathrm{exp.}}/N_{\mathrm{GB}}$ or $N_{\mathrm{FE}}/N_{\mathrm{GB}}$) are much higher than 1.0. And thus it could be concluded that the design methods in current codes underestimated the strength of the CCFST specimens and the proposed design method is necessary.

5. Conclusions

Concrete-filled steel tubes with high-strength spiral (CCFST) columns are novel hybrid columns that are extremely strong and have good ductility. The performance of CCFST columns under monotonic axial compression with different parameters, including the spacing and yield strength of the spirals and the use of longitudinal reinforcements, was investigated experimentally. An FE analysis was then performed and calibrated according to the test results. It was based on the modified hoop tensile behaviour of the spirals, the manufacturing process was considered, and a model of confined concrete with high confining stiffness was proposed. Furthermore, a parametric analysis was conducted for the FE model, and a design method for the axial load capacity was proposed. Based on the experiments and simulation presented in this paper, the following conclusions can be drawn:

Table A.1
Results calculated from the regression equations.

Specimen	f_{co} (MPa)	f_y (MPa)	$\sqrt{\alpha_s}$	ζ	$N_{exp.}$ or N_{FE} (kN)	$N_{cal.}$ (kN)	$N_{cal.}/N_{exp.}$ or $N_{cal.}/N_{FE}$
CC-20-1 (Exp.)	38.9	270.2	1.54	0.163	2070	2061	99.6%
CC-20-2 (Exp.)	38.9	270.2	1.54	0.271	2230	2271	101.8%
CC-20-3 (Exp.)	38.9	270.2	1.54	0.362	2398	2447	102.0%
CC-20-3* (Exp.)	38.9	270.2	1.54	0.362	2404	2447	101.8%
CC-40-1 (Exp.)	38.9	270.2	1.54	0.081	2096	1904	90.8%
CC-40-2 (Exp.)	38.9	270.2	1.54	0.135	2348	2008	85.5%
CC-40-3 (Exp.)	38.9	270.2	1.54	0.181	2217	2096	94.5%
CC-15-2 (Exp.)	38.9	270.2	1.54	0.362	2522	2446	97.0%
CC-15-3 (Exp.)	38.9	270.2	1.54	0.483	2686	2680	99.8%
CC-20-1 (FE)	38.9	270.2	1.54	0.163	2052	2061	100.4%
CC-20-2 (FE)	38.9	270.2	1.54	0.271	2225	2271	102.1%
CC-20-3 (FE)	38.9	270.2	1.54	0.362	2464	2447	99.3%
CC-40-1 (FE)	38.9	270.2	1.54	0.081	1847	1904	103.1%
CC-40-2 (FE)	38.9	270.2	1.54	0.135	1965	2008	102.2%
CC-40-3 (FE)	38.9	270.2	1.54	0.181	2073	2096	101.1%
Parameter analysis t = 2 mm	38.9	270.2	3.08	0.362	2092	2058	98.4%
Parameter analysis t = 6 mm	38.9	270.2	1.03	0.362	2889	2833	98.1%
Parameter analysis t = 8 mm	38.9	270.2	0.77	0.362	3235	3214	99.3%
Parameter analysis $f_y = 300$ MPa	38.9	300	1.62	0.362	2569	2534	98.6%
Parameter analysis $f_y = 400$ MPa	38.9	400	1.87	0.362	2799	2823	100.8%
Parameter analysis $f_y = 500$ MPa	38.9	500	2.09	0.362	3032	3108	102.5%
Parameter analysis $f_y = 600$ MPa	38.9	600	2.29	0.362	3252	3391	104.3%
Parameter analysis D = 90 mm	38.9	270.2	1.54	0.603	1882	2046	108.7%
Parameter analysis D = 120 mm	38.9	270.2	1.54	0.452	2167	2239	103.3%

Table B.1
Comparisons with the proposed design method and the design methods in current codes.

Specimen	$N_{cal.}$ (kN)	N_{AISC} (kN)	$N_{cal.}/N_{AISC}$ (MPa)	N_{AISC} (kN)	$N_{cal.}/N_{AISC}$ (MPa)
CC-20-1 (Exp.)	2070	1585	1.31	1793	1.15
CC-20-2 (Exp.)	2230	1585	1.41	1793	1.24
CC-20-3 (Exp.)	2398	1585	1.51	1793	1.34
CC-20-3* (Exp.)	2404	1585	1.52	1793	1.34
CC-40-1 (Exp.)	2096	1585	1.32	1793	1.17
CC-40-2 (Exp.)	2348	1585	1.48	1793	1.31
CC-40-3 (Exp.)	2217	1585	1.40	1793	1.24
CC-15-2 (Exp.)	2522	1585	1.59	1793	1.41
CC-15-3 (Exp.)	2686	1585	1.69	1793	1.50
CC-20-1 (FE)	2052	1585	1.29	1793	1.14
CC-20-2 (FE)	2225	1585	1.40	1793	1.24
CC-20-3 (FE)	2464	1585	1.55	1793	1.37
CC-40-1 (FE)	1847	1585	1.16	1793	1.03
CC-40-2 (FE)	1965	1585	1.24	1793	1.10
CC-40-3 (FE)	2073	1585	1.31	1793	1.16
Parameter analysis t = 2 mm	2092	1085	1.93	1602	1.31
Parameter analysis t = 6 mm	2889	1889	1.53	1933	1.49
Parameter analysis t = 8 mm	3235	2185	1.48	2017	1.60
Parameter analysis $f_y = 300$ MPa	2569	1665	1.54	1859	1.38
Parameter analysis $f_y = 400$ MPa	2799	1930	1.45	2086	1.34
Parameter analysis $f_y = 500$ MPa	3032	2196	1.38	2324	1.30
Parameter analysis $f_y = 600$ MPa	3252	2460	1.32	2572	1.26
Parameter analysis D = 90 mm	1882	1585	1.19	1793	1.05
Parameter analysis D = 120 mm	2167	1585	1.37	1793	1.21
			Ave. = 1.43		Ave. = 1.28
			Cov. = 0.17		Cov. = 0.14

(1) The CCFST columns showed the characteristics of high peak and residual strengths and good ductility. These characteristics were related to hybrid confinement by steel tubes and high-strength spirals.
(2) 3D laser scanning was used to measure the deformation patterns in key states. The initiation and development of local buckling and the shear-slip patterns for the CCFST columns (after fracture of spirals) were presented graphically in this paper. In addition, the deformation patterns for the SCFC and CFST columns were compared. The extra confinement (spiral or FRP tube) can reduce the outward bulging of the external steel tube.
(3) A section strip method was performed to simulate the manufacturing and loading processes. By this method, the mechanical behaviours of the spirals in the winding and springback processes were analysed. Furthermore, a modified hoop tensile constitutive model was obtained, and the modified model for spirals with a higher grade showed softening behaviour earlier.
(4) An FE analysis for the CCFST specimens was performed on the basis of modified constitutive models for concrete and spirals. And a parametric analysis was conducted to determine the influence of the strength and the dimension parameters. Finally, the design method of the axial load capacity of the CCFST was obtained by fitting the experimental results and the results from the parametric analysis.
(5) This paper demonstrates the enhancement of the spiral confinement on the performance of CCFST stubs. For a more comprehensive understanding, more studies need to be carried out, for example, axial compressive tests for a long column or eccentric compressive tests.

CRediT authorship contribution statement

Peng Feng: Writing – review & editing, Validation, Supervision, Project administration, Methodology, Funding acquisition. **Zhiyuan Li:** Writing – original draft, Visualization, Data curation. **Yichong Zou:** Writing – original draft, Visualization, Validation, Methodology, Investigation, Data curation, Conceptualization. **Jia-Qi Yang:** Writing – review & editing.

Declaration of competing interest

The authors declare that they have no known competing financial interests or personal relationships that could have appeared to influence the work reported in this paper.

Data availability

Data will be made available on request.

Acknowledgements

This work was supported by the National Natural Science Foundation of China (No. U2106219 and 51978379), and the Institute of Guo Qiang, Tsinghua University, China (No. 2019GQG1004 and 2021GQI0007).

Appendix A

See Table A.1.

Appendix B

See Table B.1.

References

[1] L.H. Han, W. Liu, Theory of concrete-filled steel tubular structures in China, in: Proceedings of the Seventh International Symposium on Structural Engineering for Young Experts, 2002, pp. 894–898.

[2] L.H. Han, W. Liu, Y. Yang, Behaviour of concrete-filled steel tubular stub columns subjected to axially local compression, J. Construct. Steel Res. 64 (4) (2008) 377–387.

[3] Z. Ou, The practice of concrete filled steel tube piers to bridges: A review, in: Progress in Industrial and Civil Engineering II, 2nd International Conference on Civil, Architectural and Hydraulic Engineering (ICCAHE 2013), 2013, pp. 1602–1605.

[4] Y. Xiao, W.H. He, K.K. Choi, Confined concrete-filled tubular columns, J. Struct. Eng. 131 (3) (2005) 488–497.

[5] M. Su, Y. Cai, X. Chen, B. Young, Behaviour of concrete-filled cold-formed high strength steel circular stub columns, Thin-Walled Struct. 157 (2020) 107078.

[6] J. Zhu, J. Chen, T. Chan, Analytical model for circular high strength concrete filled steel tubes under compression, Eng. Struct. 244 (2021) 112720.

[7] E. Ellobody, B. Young, D. Lam, Behavior of normal and high strength concrete filled compact tube circular stub columns, J. Construct. Steel Res. 62 (2006) 706–715.

[8] M. Shosuke, Recent developments on concrete-filled steel tube members in Japan, in: Proceedings of the Composite Construction in Steel and Concrete IV, Banff, Canada, 2002.

[9] L.H. Han, W. Li, R. Bjorhovde, Developments and advanced applications of concrete-filled steel tubular (CFST) structures: Members, J. Construct. Steel Res. 100 (2014) 211–228.

[10] B.T. Zheng, J.G. Teng, A plasticity constitutive model for concrete under multiaxial compression, Eng. Struct. 251 (2022) 113435.

[11] J. Chen, T. Chan, Compressive behaviour and design of compact to slender octagonal concrete-filled steel tubular stub columns, Thin-Walled Struct. 167 (2021) 108211.

[12] H. Fang, T. Chan, B. Young, Structural performance of concrete-filled cold-formed high-strength steel octagonal tubular stub columns, Eng. Struct. 239 (2021) 112360.

[13] J. Cai, Z.Q. He, Axial load behavior of square CFT stub column with binding bars, J. Construct. Steel Res. 62 (5) (2006) 472–483.

[14] Y. Wang, Y. Yang, S. Zhang, Static behaviors of reinforcement-stiffened square concrete-filled steel tubular columns, Thin-Walled Struct. 58 (2012) 18–31.

[15] Z. Tao, B. Uy, L. Han, Z. Wang, Analysis and design of concrete-filled stiffened thin-walled steel tubular columns under axial compression, Thin-Walled Struct. 47 (12) (2009) 1544–1556.

[16] J. Qian, N. Li, X. Ji, Z. Zhao, W. Cao, Experimental study on seismic behavior of composite-sectioned high strength concrete filled steel tubular columns, J. Build. Struct. 34 (5) (2013) 96–104.

[17] J. Qian, Y. Zhang, X. Ji, W. Cao, Test and analysis of axial compressive behavior of short composite-sectioned high strength concrete filled steel tubular columns, J. Build. Struct. 32 (12) (2011) 162–169.

[18] F. Ding, C. Fang, Y. Bai, Y. Gong, Mechanical performance of stirrup-confined concrete-filled steel tubular stub columns under axial loading, J. Construct. Steel Res. 98 (2014) 146–157.

[19] F. Ding, L. Luo, J. Zhu, L. Wang, Z. Yu, Mechanical behavior of stirrup-confined rectangular CFT stub columns under axial compression, Thin-Walled Struct. 124 (2018) 136–150.

[20] F. Ding, J. Zhu, S. Cheng, X. Liu, Comparative study of stirrup-confined circular concrete-filled steel tubular stub columns under axial loading, Thin-Walled Struct. 123 (2018) 294–304.

[21] P. Feng, S. Cheng, Y. Bai, L. Ye, Mechanical behavior of concrete-filled square steel tube with FRP-confined concrete core subjected to axial compression, Compos. Struct. 123 (2015) 312–324.

[22] P. Feng, S. Cheng, T. Yu, Seismic performance of hybrid columns of concrete-filled square steel tube with FRP-confined concrete core, J. Compos. Constr. 22 (4) (2018).

[23] S. Cheng, P. Feng, Y. Bai, L.P. Ye, Load-strain model for steel-concrete-FRP-concrete columns in axial compression, J. Compos. Constr. 20 (5) (2016).

[24] P. Feng, J.Q. Yang, Z. Li, FRP confined concrete: What, why, and how? in: 10th International Conference on FRP Composites in Civil Engineering. CICE2021.

[25] J.G. Teng, J.J. Wang, G. Lin, J. Zhang, P. Feng, Compressive behavior of concrete-filled steel tubular columns with internal high-strength steel spiral confinement, Adv. Struct. Eng. 24 (8) (2021) 1687–1708.

[26] J.G. Teng, J. Zhang, J.J. Wang, G. Lin, P. Feng, Concrete-filled steel tubular columns with internal confinement by high strength steel sprials, in: 8th International Conference on Steel and Aluminium Structures, ICSAS, 2016.

[27] SAC, Metallic Materials — Tensile Testing -Part 1: Method of Test at Room Temperature, GB/T 228.1-2010, Beijing, China, 2010.

[28] MOHURD, Standard for Evaluation of Concrete Compressive Strength, GB/T 50107-2010, Beijing, China, 2010.

[29] ASTM ASFT, Standard Test Method for Apparent Hoop Tensile Strength of Plastic or Reinforced Plastic Pipe by Split Disk Method, ASTM D2290-12, Philadelphia, USA, 2012.

[30] P. Feng, H. Qiang, L. Ye, Discussion and definition on yield points of materials, members andf structures (in Chinese), Eng. Mech. 34 (3) (2017) 36–46.

[31] P. Feng, Y. Zou, L. Hu, T. Liu, Use of 3D laser scanning on evaluating reduction of initial geometric imperfection of steel column with pre-stressed CFRP, Eng. Struct. 198 (2019).

[32] F. Legeron, P. Paultre, J. Mazars, Damage mechanics modeling of nonlinear seismic behavior of concrete structures, J. Struct. Eng. 131 (6) (2005) 946–955.

[33] T. Yu, J.G. Teng, Y.L. Wong, S.L. Dong, Finite element modeling of confined concrete-I: Drucker–Prager type plasticity model, Eng. Struct. 32 (3) (2010) 665–679.

[34] T. Yu, J.G. Teng, Y.L. Wong, S.L. Dong, Finite element modeling of confined concrete-II: Plastic-damage model, Eng. Struct. 32 (3) (2010) 680–691.

[35] J.G. Teng, Y.L. Huang, L. Lam, L.P. Ye, Theoretical model for fiber-reinforced polymer-confined concrete, J. Compos. Constr. 11 (2) (2007) 201–210.

[36] T. Jiang, J.G. Teng, Analysis-oriented stress–strain models for FRP-confined concrete, Eng. Struct. 29 (11) (2007) 2968–2986.

[37] Z. Wang, Structural RC Columns Reinforced with FCCC-R: Axial Compressive Behavior and Seismic Performance, Tsinghua University, Beijing, China, 2019.

[38] J.Q. Yang, P. Feng, Analysis-oriented models for FRP-confined concrete: 3D interpretation and general methodology, Eng. Struct. 216 (2020) 110749.

[39] J.Q. Yang, P. Feng, Analysis-oriented model for FRP confined high-strength concrete: 3D interpretation of path dependency, Compos. Struct. 278 (2021) 114695.

[40] Z. Li, P. Feng, J.Q. Yang, Analysis-oriented model for FRP tube-confined concrete: 3D interpretation of biaxial tube behaviour, Eng. Struct. 272 (2022) 114987.

[41] Y. Zou, Behavior of Hybrid Columns of Concrete Filled Steel Tube with High Strength Spiral Reinforcement, Tsinghua University, Beijing, China, 2020.

[42] AISC, Specification for Structural Steel Building, ANSI/AISC 360-16, Chicago, Illinois, USA, 2016.

[43] MOHURD, Techical Code for Concrete Filled Steel Tubular Structures, GB 50936-2014, Beijing, China, 2014.